Atmospheric
Chemistry
and Physics

Supplement of

A comprehensive laboratory study on the immersion freezing behavior of illite NX particles: a comparison of 17 ice nucleation measurement techniques

N. Hiranuma et al.

Correspondence to: N. Hiranuma (seong.moon@kit.edu)

S1.   Supplementary Methods

This supplementary information provides additional details for the measurement techniques of immersion freezing of illite NX particles with S1.1. suspension techniques and S1.2. dry-dispersed particle measurement techniques (both in alphabetical order as in Table 1). The discussions of measurement uncertainties of temperature and n_s for each measurement technique are also provided. We note that the uncertainty in frozen fraction (α) used in calculating n_s may not be adequate, since the sensitivity of $\Delta\alpha$ (an increase or a decrease in frozen fraction) is much higher at high temperatures which unexceptionally coincide with a low fraction of frozen illite NX.

S1.1.   Suspension techniques

Bielefeld Ice Nucleation ARraY (BINARY)

The BINARY setup is an optical freezing apparatus that makes use of the change in droplet brightness during freezing for the automated and simultaneous detection of ice nucleation in 36 microliter-sized droplets. The droplets are positioned on a hydrophobic glass slide that rests on top of a Peltier cooling stage (Linkam LTS 120). The 36 droplets are separated from each other by a polydimethylsiloxane (PDMS) spacer in order to prevent a Wegener-Bergeron-Findeisen process. For a particular illite NX concentration (0.1, 0.5, 2, 5 and 10 mg mL^{-1} based on the amount of suspended mass of illite NX sample per H$_2$O volume) at least 3 experiments with 36 drops each were conducted, resulting in a minimum of at least 108 freezing events at each concentration. The droplet temperature was calibrated based on phase transition temperatures of several compounds over the range from 0 to -40 °C and for rates between 0.1 and 10 °C min^{-1}. Details of the setup and its temperature calibration are presented elsewhere (*Budke and Koop*, 2014). In addition to this temperature calibration no further corrections were made to the dataset of observed individual droplet freezing temperatures. However, if any droplet freezing temperatures of a particular concentration were below -25 °C, this concentration was excluded from the analysis. At these temperatures, the derived n_s for different illite NX mass concentrations deviate from each other, indicating

32 that ice nucleation in these droplets was not induced by illite NX particles, but rather by ice-

33 nucleating impurities contained in the water. This lower temperature limit is also in agreement

34 with the observed 25th percentile freezing temperature value of about -26 °C for pure water

35 samples. Additionally, if at a specific temperature less than 1% of the freezing events in a

36 concentration series occur, the corresponding data point was also excluded.

37   **Experimental uncertainties:** The spread of experimentally found transition

38 temperatures in the calibration indicates a quartiles-based error of $\pm$ 0.3 °C. Assuming 10%

39 errors in the mass concentration, the droplet volume, and the frozen fraction an error of about

40 20% is associated to the active site density per mass based on Gaussian error calculation. The

41 maximal error is 35%. For the active site density per surface area an additional error has to be

42 included due to the uncertainty in the specific surface area.

43

44 **Colorado State University Ice Spectrometer (CSU-IS)**

45

46   An immersion-freezing method was used to obtain INP temperature spectra for NX-

47 illite clay, both when in bulk suspension and for size-selected particles.

48   For the bulk clay, a 0.5 wt% suspension was made in 10 mM sodium phosphate buffer

49 (at *pH* 8.7 to match the *pH* of the sample and to prevent flocculation, and filtered through a

50 0.02 µm Anotop syringe filter (Whatman)) and mixed by tumbling end-over-end at 1 cycle s^{-1}

51 for 30 min (Cole-Palmer, Roto-Torque). Measures of INP were made on this suspension and

52 on a series of 20-fold dilutions to 3.1 x 10^{-6} wt% in the same buffer.

53   Polydisperse NX-illite particles were generated for size selection using the simple

54 flask generator as described in *Tobo et al*. (2014). For collection of size-selected particles,

55 several grams of dust were placed in a 250 mL conical flask, and dust released by blowing

56 nitrogen in at the base base (~2 L min^{-1}) while agitating the flask in an ultrasonic bath. The

57 particle stream was passed through a dilution tank (N$_2$ flow rate into the tank ~5 L min^{-1}) and

58 then through a ^{210}Po neutralizer before size selection of particles with a mobility diameter of

59 500 nm in a DMA (TSI Inc., Model 3081; sheath flow: 4.5 L min^{-1}, sample flow: 1.8 L

60 min^{-1}). This stream was then divided, with 0.3 L min^{-1} passed to a condensation particle

61 counter (CPC, TSI Inc., Model 3010) and 1.50 L min^{-1} drawn through a 47 mm diameter in-

62 line aluminum filter holder (Pall) fitted with a 0.2 µm-diameter-pore Nuclepore track-etched

63 polycarbonate membrane (Whatman). Concentration of 500 nm particles was maintained at

64 around 1,500 cc^{-1} and flow was continued until 127 million particles were collected. Filters

65 and dissembled filter holders had been pre-cleaned, separately, by soaking in 10% H$_2$O$_2$ for

66 10 and 60 min, respectively, followed by three rinses in deionized water (18 MΩ cm and 0.2

67 μm-diameter-pore filtered). Filters were dried on foil in a particle-free, laminar flow cabinet,

68 as were filter holder components after excess water was removed with a gas duster.

69   After particle collection, the filter was transferred to a sterile, 50 mL Falcon

70 polypropylene tube (Corning Life Sciences), 5.0 mL of 0.2 μm-pore-diameter-filtered

71 deionized water added (which contained 1-3 INP mL^{-1} at -23 °C), and particles re-suspended

72 by tumbling for 30 min on the rotator. Measures of INP were made on this suspension and on

73 a 20-fold dilution.

74   To obtain INP temperature spectra, suspensions were first aliquoted into sterile, 96-

75 well polypropylene polymerase chain reaction (PCR) trays (Life Science Products Inc.) in a

76 laminar flow cabinet. For each dilution, 32 aliquots of 60 μL were dispensed. Trays were

77 capped with polystyrene lids (Nunc microwell plates, Thermo Fisher Scientific Inc.) and

78 transferred to CSU-IS.

79   The IS was constructed using two 96-well aluminum incubation blocks for PCR plates

80 (VWR) placed end-to-end and encased on their sides and base by cold plates (Lytron). A

81 ULT-80 low temperature bath (Thermo Neslab) circulating SYLTHERM XLT heat transfer

82 fluid (Dow Corning Corporation) was used for cooling. PCR plates were placed in the blocks,

83 the device covered with a plexiglass window and the headspace purged with 1.2 L min^{-1} of

84 filtered (HEPA-CAP, Whatman) nitrogen. Temperature was then lowered at 0.33 °C min^{-1},

85 measured using a thermistor verification probe (Bio-Rad, Hercules, CA, VPT-0300) inserted

86 into a side well. The number of frozen wells were counted at 0.5 or 1 °C degree intervals, and

87 cumulative numbers of INP mL^{-1} suspension estimated using the formula ln(f)/V, where f is

88 the proportion of droplets not frozen and V is the volume of each aliquot (*Vali*, 1971). This

89 was converted to INP g^{-1} illite and thence to INP m^{-2} illite assuming a surface area of 124 m^2

90 g^{-1} dust. For size-selected particles, mass was calculated assuming particles were spherical

91 and had a density of 2.65 g cm^{-3}.

92   **Experimental uncertainties:** The temperature uncertainty in the CSU-IS technique is

93 ± 0.2 °C (a combination of the uncertainty in the probe and the temperature variation across

94 the blocks due to gradients in cooling). Binomial sampling confidence intervals (95%) were

95 derived using as recommended by *Agresti and Coull* (formula number 2, 1998). Their ranges

96 varied according to the proportion of wells frozen. For a single well frozen out of 32 aliquots,

97 the 95% confidence interval ranged from 18% to 540% of the estimated n_s value, while for

98 31/32 wells frozen it was 53-149% of the n_s value.

99

Leeds Nucleation by Immersed Particles Instrument (Leeds-NIPI)

Picoliter (pL)-NIPI: the experimental approach employed to study freezing by illite NX particles in droplets 10's μm in diameter has been described in detail by *Broadley et al.* (2012). This instrument has been used in a number of studies of hetereogeneus ice nucleation (*Atkinson et al.*, 2013; *Murray et al.*, 2011; *O'Sullivan et al.*, 2014). Briefly, droplets of dust suspension are generated using a nebuliser and allowed to settle onto a hydrophobic coated glass slide. The droplets are sealed in oil and then transferred to a microscope cold stage where they are cooled at a controlled rate. The droplet freezing temperatures are recorded using a camera coupled to the microscope.

Microliter (μL)-NIPI: This more recently developed technique makes use of larger droplets (~1 mm) which thereforecontain a greater surface area of dust for a constant dust concentration. The μL-NIPI is sensitive to smaller values of n_s than the pL-NIPI. This instrument is described by *Atkinson et al.* (2013), *O'Sullivan et al.* (2014) and also used by *Herbert et al.* (2014) for heterogeneous ice nucleation studies. It has not previously been used for illite NX particles. Briefly, experiments involve pippetting 1 μL volume droplets of suspension onto a hydrophobic glass slide positioned on a cold stage. The cold stage is cooled by a stirling engine (Grant-Asymptote EF600) and droplet freezing is recorded using a digital camera.Values of n_s have been extended to much higher temperatures using the μL-NIPI.

The recorded images of droplets freezing for both NIPI experiments are analysed in order to determine the freezing temperature of each droplet. For the pL-NIPI the size of each droplet is also recorded. In the μL-NIPI experiments droplets are of a uniform size since they were pipetted onto the surface.

Experimental uncertainties: To calculate error in n_s the Leeds-NIPI measurement, errors from the BET surface area, the weights used to make up suspensions, dust density and estimated pipetting error to calculate an error in the amount of IN surface area per droplet were propagated. The resulting error for 0.1wt% and 1wt% suspension was ± 18.9% and ± 10.8% in n_s, respectively. The temperature error was calculated by taking the random error of the thermocouple used to measure temperature in a cold stage and propagated this with the melting point range observed for water. This resulted in a maximum error of less than ± 0.4 °C.

Mainz Acoustic Levitator (M-AL)

Inside the acoustic levitator (type APOS BA 10 from TEC59) a standing ultrasonic wave is produced by interference where drops can be levitated at the nodes. It is installed inside a walk-in cold chamber where the setup includes the acoustic levitator, a platinum-resistor thermometer Pt100 to measure the ambient temperature, a digital video camera to determine the drop sizes, and an infra-red thermometer to directly and contact-free measure the temperature of the freezing drops. These measurements require a circular spot of approximately 1 mm in diameter and, therefore, the investigated drops had sizes of 2 ± 0.2 mm in diameter. Because of their rather large volume and missing ventilated heat transfer the levitated drops cool down rather slowly while exchanging heat with the ambient air in the cold chamber. This results in a non-linear cooling rate. During the experiments with illite-NX, the temperature of pure water drops developed as follows (*Diehl et al.,* 2014):

$$T_{\mathrm{drop}}(T) = -27.050 \,^{\circ}\mathrm{C} + 27.082 \,^{\circ}\mathrm{C} \exp\left(-\frac{t}{16.374}\right) \qquad \text{(Eqn. S1)}$$

where $T_{\mathrm{drop}}(t)$ *is* the drop surface temperature, t the time. Individual drops containing polydisperse illite NX particles were levitated one after another and cooled down according to Eqn. S1. The transition from the liquid to the ice phase was clearly defined by a sudden increase of the drop temperature (because of the release of latent heat) recorded from the infra-red thermometer (*Diehl et al.,* 2014). For each particle concentration, approximately 100 drops were observed until they froze and the freezing temperatures, i.e. the lowest drop temperatures were recorded with a measuring error of ± 0.7 K. Afterwards, for temperature steps of 1 K the fractions of frozen drops were counted.

Experimental uncertainties: The uncertainties for T and n_s are $\pm 0.7 \,^{\circ}\mathrm{C}$ and $\pm 30\%$, respectively. The n_s uncertainty includes errors of the frozen fractions of drops, the specific particle surface area, the particle masses per drop, and the drop sizes.

Mainz vertical Wind Tunnel (M-WT)

In the Mainz vertical wind tunnel drops are freely floated at their terminal velocities in an air stream. Thus, ventilation and heat transfer are similar to the situation as in the real atmosphere. The wind speed is uniformly distributed around the entire cross section area up to

166   the boundary layer at the tunnel walls. This ensures that drops float in a stable fashion in the

167   observation section of the tunnel (*Szakáll et al.,* 2009; *Diehl et al*., 2011). The drop size was

168   determined from the recorded wind speed in the tunnel as it must be equal to the terminal

169   velocity of the drop to keep the drop floating in the observation section. The drop temperature

170   was calculated afterwards from the ambient temperature in the wind tunnel and the dew point

171   with an estimated error of $\pm$ 1 K. Drop sizes of 680 $\pm$ 60 μm in diameter were selected

172   because the onset of freezing was determined by direct observation (*Diehl et al.,* 2014). The

173   experiments were performed at constant ambient temperatures, i.e., the wind tunnel was pre-

174   cooled to certain temperatures in steps of 1 K. The adaption time of the drops, i.e., the time

175   after which the drop temperature was equal to the ambient temperature was 4 to 5 s (*Diehl et*

176   *al.,* 2014). Individual drops containing polydisperse illite NX particles were observed for

177   approximately 30 to 40 s. 50 drops were investigated per temperature interval and particle

178   concentration. Afterwards, the fractions of frozen drops were counted for a total observation

179   time of 30 s.

180   **Experimental uncertainties:** The uncertainties for T and n_s are $\pm$ 1 ˚C and $\pm$ 35%,

181   respectively. Similar to M-AL, the n_s uncertainty of M-WT includes errors of the frozen

182   fractions of drops, the specific particle surface area, the particle masses per drop, and the drop

183   sizes.

184

North Carolina State cold stage (NC State-CS)

186

187   The design of the NC State cold stage-supported droplet freezing assay (NC State-CS

188   for brevity) and data reduction technique is described in detail in *Wright and Petters* (2013)

189   and *Hader et al*. (2014). For the experiments reported here, aqueous suspensions ranging from

190   0.0001 to 1.0 wt% of dry illite NX powder and (18.2 MΩ cm resistivity) were prepared.

191   Droplet populations of two distinct size ranges were investigated. Picodrops were generated

192   by mixing a 15 μL aliquot of bulk suspension with squalene and emulsifying the hydrocarbon-

193   water mixture using a vortex mixer. The emulsion was poured into an aluminum dish holding

194   a hydrophobic glass slide. This resulted in between ~400 and 800 usable droplets per

195   experiment with a typical diameter $D \sim 85$ μm. Nanodrops were generated by manually

196   placing drops with a syringe needle tip on a squalene covered glass slide and letting the drops

197   settle to the squalene-glass interface. This resulted in ~80 droplets per experiment with a

198   typical diameter $D \sim 660$ μm. For all experiments the aluminum dish was cooled at a constant

199   rate of 1 ºC min^{-1} and the fraction of unfrozen drops was recorded using a microscope in

200   increments of $\Delta T = 0.17$ ℃ resolution. To account for slightly higher temperatures of the

201   squalene relative to the glass slide, a temperature calibration was applied to the nanodrop data

202   (*Hader et al.*, 2014). The resulting fraction of droplets frozen versus temperature data were

203   inverted to find the concentration of INPs using the method of *Vali* (1971):

204

205   $$c_{IN}(T) = -\frac{\ln(f_{unfrozen})}{V_{drop}}$$ (Eqn. S2)

206

207   where $c_{IN}(T)$ is the concentration of INPs per unit volume of water (m^{-3} water), $f_{unfrozen}$ is the

208   fraction of unfrozen drops at each particular temperature, and V_{drop} is the median drop volume

209   of the population. To minimize sample heterogeneity, only droplets with 78 μm $< D <$ 102 μm

210   were included in the calculation of $c_{IN}(T)$ for picodrops. No restriction was applied to the

211   nanodrops. Furthermore, the warmest two percent of data was removed after the calculation of

212   $c_{IN}(T)$ before plotting due to large uncertainty stemming from poor counting statistics (*Hader*

213   *et al.*, 2014). The nuclei content of the ultrapure water was measured in the above manner,

214   resulting in $c_{impurties}(T)$. A best fit line was determined between -20 ℃ and -35 ℃

215   (approximately a homogeneous freezing point for the size of drops used). No impurities were

216   detected at $T >$ -20 ℃. The effective INP content was determined by subtracting the nuclei

217   content in the water, $c_{impurities}(T)$, from the measured $c_{IN}(T)$ in the illite NX suspensions. For

218   most conditions $c_{impurties}(T)$ was negligible relative to $c_{IN}(T)$. The ice nucleation surface active

219   site density was then calculated via

220

221   $$n_{s,BET}(T) = -\frac{c_{IN}(T) - c_{impurities}(T)}{\rho_w w \theta_{N_2}}$$ (Eqn. S3)

222

223   where ρ_w is the density of water (997.1 kg H$_2$O m^{-3} H$_2$O), w is the mass ratio of dust and water

224   (g dust g^{-1} water), θ_{N2} is the N$_2$-based SSA obtained by BET analysis (124.4 m^2 g^{-1} dust) and

225   $n_{s,BET}$ is the BET-normalized IN active surface-site density (m^{-2} dust).

226   **Experimental uncertainties:** The thermistor embedded in the lower aluminum block

227   was capable of operating in the -40 $< T <$ 0 ℃ range with a stated tolerance of $\pm$ 1 ℃ (Model

228   TR141-170, Oven Industries). Repeatability of the temperature where 50% of pure water

229   picodrops froze via homogeneous nucleation was -35.7 $\pm$ 0.1 ℃ (n = 5, average diameter of

230   drops ~86 μm). In comparison, *Langham and Mason* (1958) report a median freezing

231   temperature of drops ~ -34.4 ℃ for this size range. The spread in $n_s(T)$ reported as $\square n_s(T) =$

7

232 [$n_{s,\text{max}}(T)$ - $n_{s,\text{min}}(T)/n_{s,\text{average}}(T)$] was $\Box n_s$(-30 °C) = 0.6 (n=4), $\Box n_s$(-25 °C) = 1.75 (n=4), $\Box n_s$(-

233 23 °C) = 1.28 (n=3) and $\Box n_s$(-20 °C) = 0.59 (n=2).

234

235 **University of Colorado Raman microscope cold stage (CU-RMCS)**

236

237   CU-RMCS has been described previously in detail (*Baustian et al.*, 2010; *Schill and*

238 *Tolbert*, 2013). Briefly, a Nicolet Almega XR Raman spectrometer has been coupled to a

239 research grade Olympus BX-51 microscope with 10x, 20x, 50x, and 100x magnification

240 objectives. This Raman microscope has been outfitted with a Linkam THMS600

241 environmental cell. Temperature of a cold stage inside the cell is controlled by a Linkam

242 TMS94 automated temperature controller with an accuracy of 0.1 K. Water partial pressure

243 inside the cell is controlled by mixing dry and humidified flows of N_2 and measured by a

244 Buck Research CR-A1 dew point hygrometer in line with the cell. In the present experiments,

245 however, droplets are isolated from the cell humidity by a layer of silicon oil.

246   To generate droplets for an immersion freezing experiment, a known wt% solution of

247 illite NX sample was aspirated into a Meinhard TR-30 glass concentric nebulizer. The

248 concentration of clay in suspensions was determined gravimetrically. Illite NX powder was

249 used as provided without any previous size selection or modification. Clay solutions were

250 mixed for at least 12 hours with a magnetic stir bar prior to use in ice nucleation experiments.

251 To mitigate gravimetric settling prior to nebulization, humidified nitrogen was vigorously

252 bubbled through the clay solutions immediately before aspiration. Humidified N_2 was used as

253 the carrier gas to prevent excess evaporation at the nebulizer nozzle. The nebulized spray was

254 directed at a hydrophobically treated fused-silica disc, and the nebulized droplets were

255 allowed to coagulate into supermicron droplets. After nebulization, a drop of silicon oil was

256 placed over the supermicron droplets, and the entire disk was transferred to the environmental

257 cell. Despite low relative humidities inside the cell, droplets inside the drop of silicon oil did

258 not visibly grow or shrink, even after sitting for 12 hours. Prior to each experiment, droplets

259 were examined under 50x magnification to ensure that suspended material was visually

260 evenly distributed between droplets. Thus, the concentration of clay in the droplets was

261 assumed to be the same as the concentration of clay in the bulk solution. Experiments were

262 video recorded under 10x or 20x magnification at 30 frames per second and freezing events

263 were identified by the sudden appearance of structure within droplets. Ice nucleation frozen

264 fractions were calculated as a function of temperature. Depending on the size of the droplets,

265 frozen fraction curves were separated into four different size bins: 10-20 μm, 20-60 μm, 60-

8

266   120 μm, and 120-200 μm (lateral diameter). These size bins span droplet volumes from ~0.3

267   picoliter to 2.5 nanoliter. In the present experiment, the droplets were cooled from

268   approximately 5 to -40 °C at a rate of 10 K min^{-1}. Errors in n_s values are based on the range of

269   surface areas available in each experiment. The temperature error for all droplets, 0.5 K, were

270   determined by repeated homogeneous freezing experiments on ultra-pure water.

271   **Experimental uncertainties:** For CU-RMCS, the errors (%) in log-scaled $n_{s,\mathrm{BET}}$

272     $(= 100 \times \dfrac{\log\left(n_{s,\mathrm{BET}}^{\mathrm{measred}}\right) - \log\left(n_{s,\mathrm{BET}}^{\mathrm{error}}\right)}{\log\left(n_{s,\mathrm{BET}}^{\mathrm{measred}}\right)})$ derived from surface area deviations were estimated as

273   4.3%.

274

275   **FRankfurt Ice Deposition freezinG Experiment (FRIDGE) diffusion cell**

276

277   FRIDGE is an isothermal static vacuum vapor diffusion chamber that freezes droplets

278   with immersed particles on a cold stage (S1.1; immersion mode operation) or nucleates ice on

279   dry particles deposited on a substrate (S1.2; default mode operation).

280   *Measurements of immersed particles*: Aerosol was generated by dry dispersion of

281   illite NX particles in air and diluted further with purified air. The particle number size

282   distribution of this aerosol in the 0.3-10 μm diameter range was measured by a TSI 3330-

283   OPS. Illite NX particles were collected by filtration of the aerosol using cellulose nitrate

284   membrane filters (Millipore, HABP04700). After sampling the filters were placed in vials

285   with 10 mL of deionized water. Particles were extracted from the filters by agitating for 10

286   min in an ultrasonic bath. It is noteworthy that the application of the ultrasonic bath and its

287   high efficiency in the washing process for particle removal were demonstrated with a similar

288   experimental setup employed by *Ardon-Dryer and Levin* (2014). About 80 droplets of 0.5 μL

289   volume each were taken from the washing solution with an Eppendorff-pipette and were

290   placed randomly on a silicon wafer on the cold stage. The temperature of the cold stage was

291   lowered by 1 °C min^{-1} and the number of drops that froze at each temperature was recorded

292   by the CCD camera and counted. This process was repeated several times with fresh droplets.

293   The actual number concentration of INP derived from this measurement builds on the drop

294   freezing concept of *Vali* (1971) as modified by *Ardon-Dryer and Levin* (2014), and is given

295   by

296

297 $$K'(T) = \frac{1}{V} \times [\ln(N_0) - \ln(N(T))] \times \frac{x}{y}$$ (Eqn. S4)

298

299 where $K'(T)$ is the cumulative INP concentration at a temperature T. The droplet volume is

300 given by V, N_0 is the total number of droplets, $N(T)$ is the number of frozen droplets at

301 temperature, T. The variable x is the volume of water used to wash the particles from the filter

302 and y the volume of air sampled through the filter.

303 **Experimental uncertainties:** FRIDGE measurement uncertainties are $T \pm 0.2$ °C and

304 $n_s \pm 40\%$ at -20 °C. The n_s error may become lower with decreasing temperature. Background

305 freezing induced by impurities in the water was observed at T < -23 °C. This background

306 freezing contributed to less than 15 % of the overall freezing in the range of -25 °C < T < -

307 23 °C and was accounted for the n_s estimation.

S1.2. Dry-dispersed particle measurement techniques

Aerosol Interaction and Dynamics in the Atmosphere (AIDA) cloud simulation chamber

Immersion freezing activity of dry illite NX particles pulverized by a rotating brush generator (PALAS, RBG1000) was investigated using AIDA-CECC. A series of expansion experiments with elevated temperature was performed in the temperature range between -27 and -35 ˚C. The results of a total of eighteen expansion experiments with ten polydisperse and eight size-selected illite NX particles (200, 300 and 500 nm mobility diameter segregated by a DMA) are reported in the present study.

AIDA-CECC consists of an 84 m^3 aluminum cylindrical vessel housed in a thermally insulated room. A mechanical pumping system is mounted directly under the AIDA vessel and used for expansion cooling, which actuates cooling during steady pressure drop from 1000 to 800 mb (*Möhler et al.*, 2003). During the expansion cooling experiment controlled by a mechanical pump, the cooling rates of gas temperature in the vessel typically decrease from ~5 to <0.1 ˚C min^{-1}. The conditions in the vessel, such as temperature and relative humidity, can be continuously homogenized by a mixing ventilator installed on the base of the vessel. The chamber conditions are also monitored by temperature sensors (*Möhler et al.*, 2003) and tunable diode laser (TDL) water vapor absorption measurement (*Fahey et al.*, 2014) prior to and while running each experiment. The use of AIDA for both immersion mode and deposition mode freezing experiment is described in detail in previous reports (e.g., *Hiranuma et al.,* 2014a and 2014b, respectively) so only a brief description is provided here.

For the immersion mode experiment, spontaneous formation of water droplet occurs at water saturation while continuously cooling. Thereafter, water supersaturation condition in the vessel is maintained by controlled mechanical expansion. At droplet activation, most of clay mineral particles are presumably immersed in water drops leading to droplet-freezing at a characteristic temperature (*Hiranuma et al.*, 2014b). Thus, within our definition of singular freezing, immersion ice nucleation activity of clay minerals solely depends on temperature.

Temporal evolution of size distribution and associated particle phase is measured using the welas optical spectrometers (PALAS, Sensor series 2300 and 2500; *Benz et al.*, 2005) and a light scattering instrument, *Streulicht-intensitätsmessungen zum optischen Nachweis von Eispartikeln*, (SIMONE in *German*; *Schnaiter et al.*, 2012) that are directly

11

mounted to the wall of the AIDA vessel. Two independent sensors of a welas deployed on the bottom vessel of AIDA in side by side position are used together to measure ice crystal size distributions over the size range of 0.5 to 150 μm optical diameter every 5 s. Assuming spherical shape of particles, the optical diameter is equivalent to a volume equivalent geometric diameter. The droplet-ice threshold diameter, D_{thresh}, is determined by SIMONE depolarization measurements (*Schnaiter et al.*, 2012). The total ice number was calculated by summing ice numbers above the observed D_{thresh}, typically ~30 μm diameter. For the immersion experiments, we typically observe a full activation of droplets (i.e. number of droplets, $N_{droplet}$ > number of aerosols, N_{ae}), but in case of incomplete droplet activation (i.e. $N_{droplet}$ < N_{ae}), the total geometric surface is normalized to a droplet number measured by a welas-OPC.

Experimental uncertainties: Temperature and humidity uncertainty is ± 0.3 ˚C and ± 5%, respectively (*Möhler et al.*, 2003; *Fahey* et al. ,2014). The uncertainty involved in the n_s estimation for immersion freezing in AIDA-CECC was previously estimated as 35% (*Steinke et al.*, 2011).

CSU Continuous Flow Diffusion Chamber (CSU-CFDC)

CSU-CFDC operating principles are described in the earlier works of *Rogers* (1988), *Rogers et al.* (2001) and *Eidhammer et al.* (2010). The current versions of CSU-CFDC used in ground based (CFDC-1F) and aircraft studies (CFDC-1H) are geometrically identical and composed of cylindrical walls that are coated with ice via flooding and expelling water from the chamber when the walls are set at a controlled temperature of ~ -27 °C before each experimental period. The plate separation is 1.12 cm prior to ice application, which has a typical thickness of 0.015 cm. The chamber is divided into two sections vertically, separated by a Delrin collar. A temperature gradient between the colder (inner) and warmer (outer) ice walls in the upper 50 cm section creates an ice supersaturated field into which an aerosol lamina is directed. The Delrin inlet manifold has a stainless steel knife edge ring threaded into it, so that aerosol flow is directed centrally between two sheath flows of clean and dry air. The ratio of aerosol and sheath flows can be varied, but typically the aerosol lamina represents 15% of the 10 L min^{-1} total flow. Ice crystals forming on ice nuclei in the growth region of the chamber enter the lower 30 cm "evaporation" section of the chamber where the two walls are held equivalently to the original low (inner) wall temperature. When the temperature gradient

373 in the growth section is adjusted to create water supersaturated conditions that activate cloud

374 droplets, these will evaporate to haze sizes in the evaporation section, at least up to some RH_w

375 where they survive, referred to by many as the droplet breakthrough RH_w. Until that high

376 RH_w, only ice crystals and haze particles will exit the CFDC. Upstream of the CFDC, aerosol

377 particle concentrations are measured by a CPC, sometimes after size selection with a DMA.

378 Small numbers of large aerosol particles are removed just in advance of the CFDC inlet

379 manifold using dual single-jet impactors typically set to cutpoint sizes between 1.5 and 2.4

380 μm depending on the nature of the experiment. Ice crystals and aerosols exiting the CFDC at

381 sizes above approximately 500 nm are counted with an OPC, where the two populations are

382 readily distinguished in different size modes. For the data collected in this work, we counted

383 all particles in size bins above 3 μm as ice particles.

384 Present CFDC-1F measurements were focused into 5-10 min periods of sampling

385 alternating with periods in which the aerosol sample was filtered in order to determine

386 background frost influences on ice particle counts in the OPC, as described in a number of

387 prior publications. Background counts were quite low, and so were subtracted as a simple

388 average of filter periods before and after sampling.

389 Polydisperse illite NX particles were generated for size selection using the simple flask

390 generator as described in *Tobo et al.* (2014). For collection of size-selected particles, several

391 grams of dust were placed in a 250 mL conical flask, and dust released by blowing nitrogen in

392 at the base (~2 L min^{-1}) while agitating the flask in an ultrasonic bath. The particle stream was

393 passed through a dilution tank (N_2 flow rate into the tank ~5 L min^{-1}) and then through a ^{210}Po

394 neutralizer before size selection of particles with a mobility diameter of 500 nm in a DMA

395 (TSI Inc., Model 3081; sheath flow: 4.5 L min^{-1}, sample flow: 1.8 L min^{-1}). This stream was

396 then divided, with 0.3 L min^{-1} passed to a CPC (TSI Inc., Model 3010) and 1.50 L min^{-1}

397 drawn by the CFDC. The activated fraction was calculated by taking the ratio of the ice

398 crystal number concentration to the total particle number concentration measured with the

399 CPC.

400 For comparison with other IN instruments measuring in the immersion mode, we

401 follow *Sullivan et al.* (2010a and 2010b) and a number of other papers from the CSU group in

402 processing aerosol at $RH_w \approx 105$ %, with the understanding that higher active fractions of

403 mineral dusts have been noted in processing up to about 110% RH_w (*Petters et al.*, 2009;

404 *DeMott et al.*, 2011). We did not raise RH_w to these higher levels in these studies so that we

405 could avoid any influence of droplet breakthrough. We do now report that for representative

406 atmospheric mineral dusts, activation at 105% RH_w likely underestimates the active fraction

407 measured at 109% RH_w by the CFDC by a factor of 3 across a broad temperature range

408 (*DeMott et al.* 2014).

409   Particle losses in upstream tubing, the aerosol impactor, and the inlet manifold of the

410 CFDC have been previously estimated as 30% of total condensation nuclei when sampling

411 ambient air (*Rogers et al.* 2001), but only 10% for aerosols in the 100 to 800 nm size range

412 based on laboratory tests (*Prenni et al.* 2009). We did not correct for such losses in the ice

413 nuclei data for 500 nm particles reported for the CFDC.

414   **Experimental uncertainties:** The thermodynamic conditions in the CFDC are

415 inferred based on measurements of chamber pressure, wall temperatures and flow rates.

416 Results are reported for the calculated average aerosol lamina position. The solution for the

417 lamina position, and thus its temperature and supersaturation, requires numerical solution

418 (*Rogers,* 1988), thus making the calculation of uncertainty in the conditions more complex

419 than propagation of error. *Richardson* (2009) used Monte-Carlo methods to estimate the

420 uncertainty in reported lamina temperature and supersaturation, assuming the typical 1 °C

421 temperature variation along the length of the CFDC cylindrical walls. On this basis,

422 temperature uncertainty is $\pm$ 0.5 °C at the reported CFDC processing temperature,

423 independent of processing temperature. Supersaturation uncertainty was found by *Richardson*

424 (2009) to depend inversely on temperature. This uncertainty may be approximated by the

425 relation $\Box RH_w$ (%) = 21.8 - 0.08 *T* (in Kelvin). Thus, $\Box RH_w$ uncertainty is $\pm$ 1.6, 2 and 2.4 %

426 at -20, -25, and -30 °C, respectively. This temperature uncertainty propagates into and n_s

427 uncertainty of $\pm$ 60% at any temperature. This dominates over the variation in N_{ice} at any

428 temperature when N_{ice} is determined for statistically meaningful sample periods, as reported.

429

430 **ElectroDynamic Balance (EDB) levitator**

431

432   The EDB setup was used for investigation of the contact and immersion freezing of

433 levitated supercooled water droplets colliding with the illite particles. The setup used for the

434 contact freezing experiments is described in detail by (*Hoffmann et al.*, 2013a and 2013b) and

435 therefore only briefly explained here. The centerpiece of the setup is an electrodynamic

436 balance (EDB) for levitating charged water microdroplets. The droplets with diameter of 90

437 μm are produced by a piezoelectric injector (GeSIM model A010-006 SPIP, cylindrical

438 housing) and charged via induction to the value of 1 pC (*Rzesanke et al.*, 2012). The aerosol is

439 generated by a fluidized bed generator operated with synthetic air followed by a multistage

440 impactor to eliminate the super micron particles from the aerosol flow. Specifically, the multi-

441 orifice rotating stage cascade impactor (LPI-ROT 25/0018, HAUKE) operated with five

442 impactor stages (largest cut-off diameter 2 μm) was used as described in *Hoffmann et al.*

443 (2013b). Only particles of the desired electrical mobility diameter (750, 550 and 320 nm, as

444 preselected by Differential Mobility Analyzer, TSI Inc., Model 3081) were allowed to enter

445 EDB. After EDB, the particle number concentration was counted by an Ultrafine

446 Condensation Particle Counter (UCPC, TSI Inc., Model 3776).

447 　　　　To perform immersion freezing experiments we have modified the setup in the

448 following way. The supercooled water droplet was exposed to the flow of the aerosol particles

449 only for a limited time t_1. During this time the droplet, if not frozen via contact nucleation

450 mechanism, has collected average number of particles equal to the product of collision rate

451 (calculated theoretically) and the time t_1. After that, the aerosol particles were removed from

452 the flow by switching on the electrostatic precipitator installed just in front of EDB. For $t > t_1$

453 the droplet can only freeze via the immersion freezing pathway induced by the particles it has

454 already collected during $t < t_1$.

455 　　　　To compare contact and immersion freezing results we calculate the ice nucleation

456 active surface-site density, n_s, which is given by the following equations:

457

458 　　　　$$t < t_1 \text{(contact mode)}: n_s(T) = -\frac{\ln(1-f_{ice}(T))}{S_{IN}n_c t} = \frac{e_c}{S_{IN}}$$ 　　　　(Eqn. S5)

459 　　　　$$t > t_1 \text{(immersion mode)}: n_s(T) = -\frac{\ln(1-f_{ice}^*(T))}{S_{IN}n_c t_1 t}$$ 　　　　(Eqn. S6)

460

461 where f_{ice} is the frozen fraction after time t, e_c is the probability of freezing on a single contact,

462 n_c is a collision rate, S_{IN} is surface area of a single ice-nucleating particle, f_{ice}^* is a fraction of

463 droplets frozen heterogeneously after the aerosol flow was switched off.

464 　　　　**Experimental uncertainties:** The temperature uncertainty is $T \pm 0.2$ °C, and the

465 uncertainty of the freezing probability is $e_c \pm 35\%$. The uncertainty for n_s depends on the

466 uncertainty of the BET surface. Assuming a BET uncertainty of 10-20%, the uncertainty is n_s

467 $\pm 50\text{-}69\%$.

468

Fast Ice Nucleus CHamber (FINCH)

FINCH is an online instrument in which aerosol particles are activated to ice crystals under different freezing temperatures and supersaturations. It consists of a chamber (stainless steel tube, 80 cm in length, 8.6 cm inner diameter) for which the wall can be cooled down to temperatures between 0 and -65 °C. Inside the chamber a specific supersaturation and temperature is reached by mixing the sample flow of ambient aerosol with a warm moist and a cold dry airflow (*Bundke et al.*, 2008). By changing the flow rates and/or temperatures of the individual airflows the chamber supersaturation and freezing temperature can be varied relatively quickly. Ice-nucleating particles entering the chamber are activated and grow to sizes of a few micrometers. At the end of the growth tube they are counted in an optical particle counter (OPC) similar to the detector described in *Bundke et al.* (2010) (405 nm wavelength laser with a power of 100 mW). It is able to distinguish between water droplets and ice crystals by analyzing the polarization ratio of the scattered circular polarized light (P44/P11 ratio of the scattering matrix; *Hu et al.*, 2003) and detects the auto-fluorescence following from excitation of the grown particles with UV light, which is an indication for biological particle material.

The presented FINCH illite NX dataset was obtained during a joint campaign with LACIS at the Leibniz Institute for Tropospheric Research (TROPOS) facility. Therefore the aerosol generation is identical as described for the LACIS experiments (see below). Size-selected illite NX particles of 500 nm in diameter were fed into FINCH, which was operated at a saturation ratio above water saturation and at temperatures between -21 and -28 °C. The frozen fraction, α, was calculated by division of the N_{ice} detected by FINCH at a certain freezing temperature and the number concentration of all particles, which was measured in parallel to FINCH by a CPC (TSI Inc., Model 3010).

Experimental uncertainties: The FINCH uncertainties for the freezing temperature are in the range of ± 1.5 °C and ± 30% for n_s. A potential systematic over-estimation of the freezing temperature due to imperfect mixing of the individual airflows are a matter of current investigations.

FRankfurt Ice Deposition freezinG Experiment (FRIDGE) diffusion cell

FRIDGE is an isothermal static vacuum vapor diffusion chamber that freezes droplets with immersed particles on a cold stage (S1.1; immersion mode operation) or nucleates ice on dry particles deposited on a substrate (S1.2; default mode operation).

Dry particle measurements: The default mode operation of FRIDGE provided data at -18 and -25 °C (a total of ten data points with five points at each temperature). INPs were collected from the dry illite NX particles in AIDA by electrostatic precipitation of the particles onto silicon wafers of 45 mm diameter. After sampling the wafers were placed on the cold table in the FRIDGE isothermal chamber (~500 mL volume; *Klein et al.*, 2010), which was then evacuated. Upon inflation of water vapor into the chamber ice crystals grew on the INP, were photographed by a CCD camera, and were counted automatically for around 100 s. It is assumed that one ice crystal represents one INP active at the selected temperature and vapor pressure. Crystals can be evaporated by evacuation of the chamber, and the measurement can be repeated at another temperature and/or supersaturation. The cold stage temperature can be regulated from 0 to -35 °C.

Experimental uncertainties: FRIDGE measurement uncertainties are $T \pm 0.2$ °C and $n_s \pm 40\%$ at -20 °C. The n_s error may become lower with decreasing temperature.

Leipzig Aerosol Cloud Interaction Simulator (LACIS)

LACIS was used in its immersion freezing mode (*Hartmann et al.*, 2011) to study immersion freezing efficiency of illite NX particles. LACIS measurements were performed on size segregated particles. Particle generation was done using a similar setup as e.g. described in *Wex et al.* (2014). In short, illite NX particles were made airborne using a fluidized bed. Subsequently, particles larger than those which should be examined were removed from the aerosol using a micro orifice uniform deposition impactor (MOUDI, MSP Corporation, USA, Model 100R) and a cyclone. Downstream, a neutralizer established a bipolar equilibrium charge distribution on the particles. Then particles were size-selected by a DMA (Type Vienna Hauke medium; aerosol to sheath air flow ratio of 1:10), and selected particle sizes were 300, 500 and 700 nm. The aerosol was then provided for further analysis.

530   The before mentioned removal of larger particles was done to minimize the number of

531   multiply charged particles that pass the DMA, and measurements with a UHSAS (Ultra-High

532   Sensitivity Aerosol Spectrometer, DMT) behind the DMA were done to confirm that the

533   number of multiply charged particles could be neglected.

534   Size-selected aerosol particles were also fed into a CPC (TSI Inc., Model 3010), and

535   into LACIS. LACIS is a flow tube, consisting of 7 sections where each is 1m long. Each

536   section can be temperature controlled separately. Temperatures can go down to -40 °C. Before

537   entering the flow tube, by use of a humidifier (Perma Pure, PH-30T-24KS), the sheath air

538   stream is hydrated such that droplets form on the aerosol particles upon cooling, i.e. while

539   passing through the flow tube. The droplets can subsequently freeze, depending on the nature

540   of the immersed aerosol particle and the adjusted temperature. At the LACIS outlet, a home-

541   built optical particle spectrometer (*Clauss et al.*, 2013) is used to determine if the arriving

542   hydrometeors are liquid droples or frozen ice crystals. This information then is used to derive

543   a frozen fraction, α.

544   **Experimental uncertainties:** The temperature uncertainty is $T \pm 0.3$ K, the

545   uncertainty of the measured α is on average $\pm 27.4\%$. The uncertainty in n_s was calculated

546   accounting for this measurement uncertainty and for the uncertainty related to the width of the

547   transfer function in the DMA, which was assumed to be 5%. The resulting uncertainty in n_s

548   derived from LACIS data is 28%.

549

550   **Meteorological Research Institute Dynamic Controlled Expansion Cloud-simulation**

551   **Chamber (MRI-DCECC)**

552

553   The DCECC at Meteorological Research Institute (MRI) in Tsukuba, Japan (*Tajiri et*

554   *al.*, 2013) was used to investigate immersion freezing properties of dry illite NX particles. The

555   DCECC can simulate quasi-adiabatic expansions by synchronously controlling air pressure

556   and inner wall temperature of the chamber vessel. MRI-DCECC warrants experiments with

557   atmospherically relevant droplet sizes as well as controllable droplet onset temperature

558   ($T_{\text{droplet,onset}}$) and supersaturation conditions resulting in freezing of particles in water droplets.

559   Dry illite NX particles were aerosolized by a rotating brush generator (PALAS, RBG1000)

560   and injected into the ventilated 1.4 m^3 chamber vessel. All experiments were performed by

561   employing a constant cooling rate of about -3 °C min^{-1} (equivalent to the updraft rate of about

562   5.0 m s^{-1}) from initial gas temperature typically about 5 °C. The DCECC is equipped with

563   various devices, such as an SMPS, a welas-OPC, an APS and a CPC, for sensing cloud

564   formation and measuring size distributions and shapes of aerosol and cloud particles from

565   0.01 to several hundred micrometers in size. As these instruments were also employed at

566   AIDA-CECC, the procedures to calculate the total ice number and total geometric surface

567   were also consistent with AIDA measurements.

568   **Experimental uncertainties:** The temperature uncertainty in MRI-DCECC is $T \pm 1.0$

569   °C for the evacuation rate corresponding to 5.0 m s^{-1}. The 40% uncertainty for n_s was derived

570   from the errors in the measurements of N_{ice} by a welas (20%; *Möhler et al.*, 2006) and surface

571   area estimation (34%). More specifically, the uncertainty for surface area estimation was

572   derived from the relative standard deviation of the 10 s time-averaged welas surface

573   measurements for approximately 5 min prior to expansion experiments (i.e., MRI02_131001a,

574   MRI02_131003b and MRI02_131004).

575

576 **Portable Ice Nucleation Chamber (PINC)**

577

578   PINC operation principle is based on the Continuous Flow Diffusion Chamber

579   (*Rogers*, 1988). Two flat parallel plates (568 x 300 mm) whose inner walls coated with ice

580   before each experiment are temperature controlled so as to apply a temperature gradient

581   between the ice layers leading to a supersaturation with respect to ice and water. This allows

582   ice crystals to form and grow on ice nuclei in the water sub-saturated (RH$_w$ < 100 %) and

583   supersaturated (RH$_w$ > 100 %) regimes thus inferring deposition and condensation freezing

584   respectively. Any water drops that may form will evaporate in the evaporation section

585   downstream of the freezing chamber. Upstream of PINC, aerosol particles are counted with a

586   CPC after flowing through an impactor with a D_{50} cutoff at 0.91 μm aerodynamic diameter

587   (*Chou et al.*, 2011). The ice crystals are counted with an OPC at the exit of PINC and are

588   distinguished from the small, unactivated aerosol particles by their size. For the data collected

589   in this work, we counted all particles in size bins above 2 μm to be ice particles since the illite

590   NX particles we sampled were 500 and 1000 nm in diameter. Measurements conducted for 3

591   min before each sample and one minute after a sample were averaged in order to determine

592   the background signal in the OPC. These values were then subtracted from the IN

593   concentrations obtained during sample measurement to correct for the background. Further

594   details on the PINC design and operation are described in *Chou et al.* (2011) and *Kanji et al.*

595   (2013).

596   Polydisperse illite NX particles that were suspended in the 4 m^3 volume aerosol buffer

597   chamber were size-selected using a DMA and counted using a CPC after which they were

598   sampled by PINC. The activated fraction is calculated by taking the ratio of the ice crystal

599   number concentration to the total particle number concentration measured with the CPC.

600   Particles with diameters 500 and 1000 nm were size-selected using the Maxi-DMA developed

601   at the TROPOS and described in more detail elsewhere (*Raddatz et al.*, 2013).

602   For comparison with other IN counters measuring in immersion mode, only IN data

603   taken by PINC at $RH_w \geq 104$ % and below the RH_w at which droplets survive past the

604   evaporation section ($RH_{w,ds}$), are presented. For each temperature, RH was scanned

605   continuously from $RH_{ice} = 100$ % up to $RH_{w,ds}$. $RH_{w,ds}$ lies for T = -20 °C at 105 % and at -38

606   °C at 109 %.

607   Particle losses in the tubing and the impactor upstream of PINC were accounted for by

608   a particle loss curve determined for kaolinite particles with a mobility diameter between 500 –

609   950 nm. As such the data for 500 and 1000 nm particles have been corrected for losses

610   through the impactor of 25 and 60% respectively.

611   At lower temperatures, the results show reasonable agreement with AIDA and LACIS

612   measurements, however at higher temperatures (-25 °C) we find that for the 1000 nm particle

613   we underestimate the n_s compared to LACIS for example. The reason for this is that we do not

614   have enough residence time in the growth and nucleation section of PINC (residence time of

615   4-5 s) to fully activate the particles into droplets and as such underestimate the activated

616   fraction in immersion mode. The way to compensate for this would be to sample at higher

617   RH_w (as we do for lower temperatures), but at higher temperatures we are limited by the water

618   drop survival line ($RH_w = 105$%) so we cannot compensate for the short residence time by

619   taking data points at higher RH_w. As such, data taken for immersion freezing at higher

620   temperatures could mean that we are underestimating immersion freezing, or rather be

621   reporting deposition nucleation or condensation freezing.

622   **Experimental uncertainties:** Temperature uncertainties are on the order of ± 0.1 ˚C

623   resulting in a relative uncertainty of ± 2% in RH. The temperature uncertainty results in a

624   variation across the sample lamina of ± 0.4 ˚C. Uncertainty in N_{ice} (From OPC) is 10% and

625   surface area estimate is about 25% resulting in an uncertainty in n_s of ± 27%.

626

PNNL Compact Ice Chamber (PNNL-CIC)

Heterogeneous ice nucleation properties of illite NX dust particles generated by the small-scale powder disc-disperser (SSPD, TSI, Model 3433) were investigated using ice nucleation chamber located at Atmospheric Measurement Laboratory, an atmospheric sciences laboratory at Pacific Northwest National Laboratory (PNNL), WA., USA. The working principle of PNNL compact ice chamber (PNNL-CIC) has been described in the literature (*Stetzer et al.*, 2008; *Friedman et al.*, 2011; *Kulkarni et al.*, 2012); its design and experimental details are as follows. PNNL-CIC is a continuous flow diffusion chamber consisting of two flat, vertical parallel aluminum plates that are cooled and covered with a layer of ice. The chamber also has an evaporation section attached at the bottom of the chamber to remove water droplets. The chamber design ensures that aerosols are exposed to constant temperature and RH_{ice} over the length of the chamber. Saturation vapor pressures over ice and water are calculated using formulations published by *Murphy and Koop* (2005). The chamber wall temperatures are controlled by using two external cooling baths (Lauda Brinkmann Inc.), and temperature data are logged using the National Instrument CompactRIO programmable automation controller (cRIO-9114 combined with cRIO-9022). The chamber plates are temperature controlled independently to develop a linear temperature gradient across them, which according to the principle of thermal gradient diffusion theory, produces a supersaturation profile between the plates (e.g., *Rogers et al.*, 1988). Recently we modified the evaporation section design, such that this section now has separate cooling bath and its temperature is independently controlled. Temperature of the evaporation section is typically maintained at ~ -32 °C. At the beginning of the experiment, the chamber walls are coated with an ~0.5 mm thick ice layer, and the temperature gradient is set at zero, which creates ice-saturation conditions inside the chamber (RH_{ice} = 100 %), Then, the refrigeration system cools one plate and warms the other to increase the RH_{ice}. The total flow used is 11 L min^{-1}; sheath and sample flows used were 10 and 1 L min^{-1}, respectively, which limits the aerosol residence time to ~12 s within the CIC. Ice nucleates on the aerosol particles and the newly formed ice crystal grows to a size greater than the original aerosol size, and ice crystals >3 μm exiting the chamber are counted with an OPC (CLiMET, model CI-3100). The ice active fraction was calculated as the ratio of number of ice crystals measured by the OPC to the condensation nuclei available for nucleation. Background ice nuclei concentrations were calculated to estimate the lower detection limit of an α. The lower detection limit of α was <0.01 %. To

660   make sure our background IN concentrations are less than 0.01 %, we restrict our

661   experimental time to less than 3 hours.

662   **Experimental uncertainties:** Temperature uncertainty is ~ ± 0.3 ˚C. For n_s the

663   uncertainty arises from N_{ice} measurement and surface area estimation. The resulting error is ~

664   ± one order of magnitude at any $n_s(T)$ space.

665

666   **Zurich Ice Nucleation Chamber with Immersion Mode Cooling chAmber (IMCA-ZINC)**

667

668   ZINC is a parallel plate CFDC type chamber developed by *Stetzer et al.* (2008)

669   following the design described in the work of *Rogers* (1988). The chamber inner-walls are

670   coated with ice prior to experiments. Under equilibrium conditions, linear temperature and

671   vapor pressure gradients are established between the warmer and colder walls creating

672   supersaturated conditions with respect to ice or water in the chamber volume. The two

673   chamber walls are separately temperature-controlled by two cryostats (Lauda RP890).

674   Independent temperature control of the two walls enables experiments at relative humidity

675   conditions ranging from ice saturation until several hundred per cent of water saturation. An

676   evaporation section, where both walls are kept at the same temperature to create ice saturated

677   but water-sub-saturated conditions, is able to evaporate potentially formed droplets, before

678   being sampled by an OPC. Deposition mode experiments are conducted by scanning through

679   relative humidity space while keeping the experimental temperature constant by increasing the

680   temperature gradient between the two wall plates. The streamline of the injected illite NX

681   particles (generated by a combination of a TSI fluidized bed, a series of URG cyclone

682   impactors and a TSI DMA; *Welti et al.*, 2009) is maintained at approximately the center

683   position between the ice coated walls by two layers of particle-free sheath air. At the exit of

684   ZINC, ice crystals are detected and distinguished from inactivated particles by size using an

685   OPC (Climet Cl-3100). The particle concentration introduced into the experiment is detected

686   with a butanol-CPC (TSI 3010).

687   The IMCA chamber was developed by *Lüönd et al.* (2010) as a vertical extension to

688   ZINC and has the same parallel plate geometry. The walls are layered with continuously

689   wetted filter papers and temperature controlled. Similar to ZINC, a horizontal temperature

690   gradient is applied to create supersaturation with respect to water between the walls. When

691   entering IMCA, particles are exposed to 120% saturation with respect to water at 40 °C to

692 trigger droplet formation and growth. Subsequently, a vertical temperature gradient is

693 established to cool the formed droplets down to the experimental temperatures prevailing in

694 ZINC. For immersion freezing experiments ZINC is held at water saturated conditions to

695 prevent evaporation or droplet growth. Droplets and ice crystals are detected in line before

696 entering ZINC's evaporation section using the Ice Optical DEpolarization detector (IODE)

697 described in *Nicolet et al.* (2010). IMCA-ZINC combination mimics an atmospheric pathway

698 where particles are activated as cloud droplets at temperatures above 0 °C, subsequently

699 cooled and exposed to sub-zero temperatures at which freezing can occur.

700 **Experimental uncertainties:** Temperature uncertainty is $\pm$ 0.4 ˚C. The uncertainties

701 in $n_s(T)$ are propagated from the uncertainties in IODE and the surface area ($\pm$ 25%).

S2.   Supplementary Figures

An X-ray diffraction measurement was performed by a Panalytical X`Pert Pro device (fixed divergence, 40 kV, 30 mA, CuK$_a$ exication). For data analysis the X`Pert Pro software was applied. While we successfully identified several different forms of orthoclase (KAlSi3O8) with some Na inclusion, we cannot specify the type of K-feldspar polymorphs (e.g., microcline). Therefore, we define the feldspar as orthoclase or sanidine in the present study.
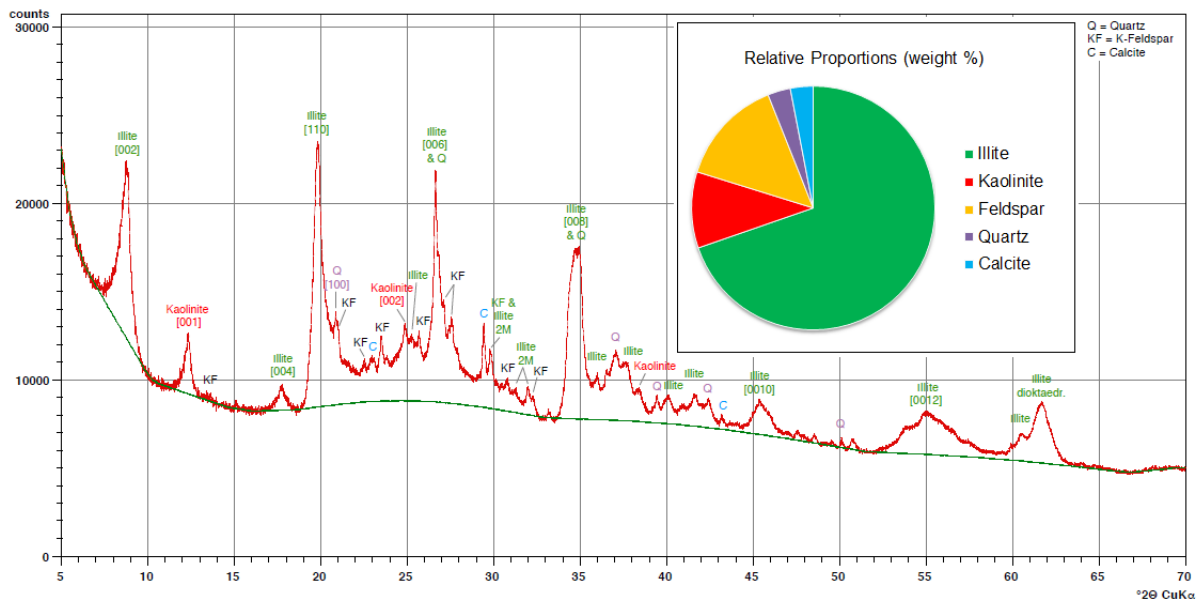

Figure S1. X-ray diffraction spectrum of the illite NX sample. The pie chart reflects the wt% presented in Table 2 (*this study*).

713   Spectra of $n_s(T)$ (Figs. 4 and 5) can be converted to $n_m(T)$ spectra using Eqn. 4. Spectra

714   of $n_m(T)$ are presented in Fig. S2. Illite NX is insoluble and is a non-swelling dust, so $n_m(T)$

715   may not correctly represent its immersion freezing efficiency (*Murray et al.*, 2012). However,

716   we note that this IN mass reflects the most direct representation of suspension measurements

717   since conversion of α into $n_{m,sus}(T)$ requires only one value, which is SSA (Eqn. 4).
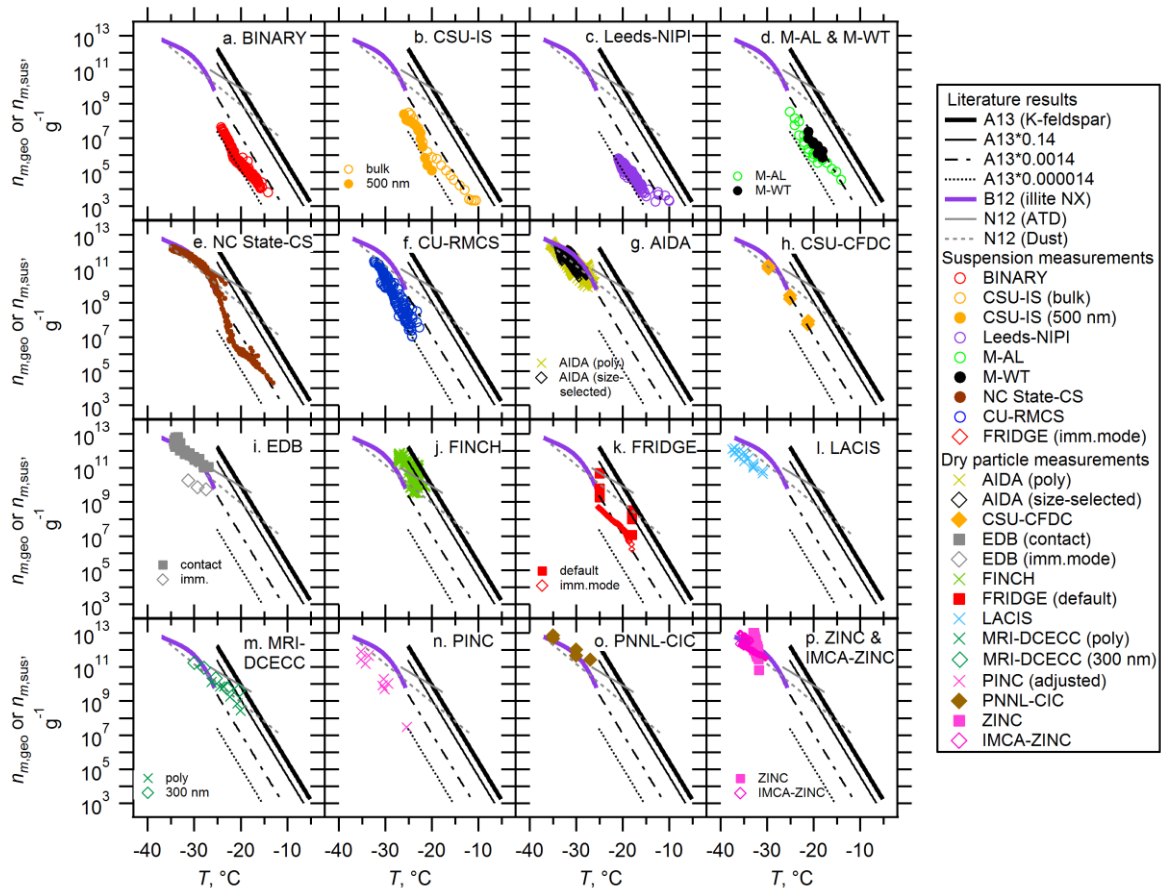
718
719   Figure S2. Inter-comparison of seventeen instruments with $n_{m,geo}$ or $n_{m,sus}$ (for dry-dispersed particle and
720   suspension measurements, respectively). Note that M-AL and M-WT results are presented in single panel (d). In
721   (k), FRIDGE results of default (solid square) and imm.mode (open diamond) are presented. Both ZINC (solid
722   square) and IMCA-ZINC (open diamond) data are shown in (p). Reference immersion freezing $n_s(T)$ spectra for
723   illite NX (B12), K-feldspar (A13), ATD and desert dusts (Dust) (N12) are also shown (See Sect. 3.2).

724   The linear space n_s average as presented in Fig. 8 may bias the fit to higher n_s values.

725   Therefore, we present T-binned $n_{s,\mathrm{BET}}(T)$ and $n_{s,\mathrm{geo}}(T)$ spectra averaged in the 'log space' in

726   Fig. S3a and b, respectively. In a similar way to the presentation in Fig. 8, panels i, ii and iii of

727   Fig. S3 show T-binned data averaged in the log space of all seventeen instruments, all

728   suspension type measurements, and all measurements that involved dry particles, respectively,

729   while panel iv shows a comparison between suspension and dry-particle measurements. To be

730   comparable with Fig. 8, the data from 'EDB (contact)' and 'ZINC' (*Welti et al.*, 2009) were

731   not used to generate T-binned data. As can be seen in both Fig. S3 and Fig. 8, there seems a

732   different trend between suspension and dry-dispersed particle measurements for this mineral dust.

733   Thus, the choice of averaging procedure does not influence our data interpretation of the

734   observed deviation (i.e., n_s from dry-dispersed methods $> n_s$ from suspension methods) in this

735   study.
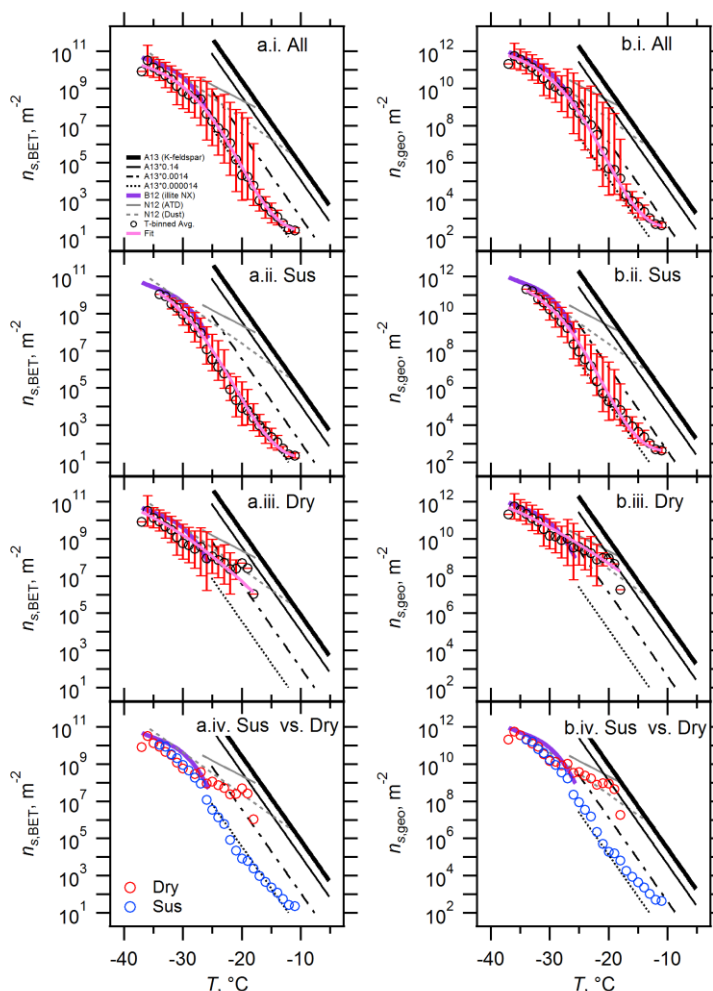
736
737   Figure S3. T-binned spectra based on $n_{s,\mathrm{geo}}$ (a) and $n_{s,\mathrm{BET}}$ (b). T-binned data (i.e., average in the log space with 1
738   °C bins for -37 °C $< T <$ -11 °C) of $n_s(T)$ spectra are presented for (i) All interpolated dataset (All), (ii)
739   Suspension measurements (Sus), (iii) Dry-dispersed particle measurements (Dry), and (iv) comparison between
740   Sus and Dry. Red sticks represent maxima (positive direction) and minima (negative direction). Literature results
741   (B12, A13, and N12) are also shown.

742   Figures S4 depicts the n_s diversity in $\log(n_{s,\text{ind.}})/\log(n_{s,\text{fit}})$, which represents the ratio of

743   the individual measurements ($n_{s,\text{ind.}}$) to the log fit line to either all data [All (log)], the

744   suspension data [Sus (log)] or the dry-dispersed particle data [Dry (log)] as $n_{s,\text{fit}}$. The

745   interpolated T-binned data (i.e., interpolated data points in Figs. 4 and 5) are used for $n_{s,\text{ind.}}$.

746   The fit in the log space, which is derived from the parameters summarized in Table 3, is used

747   as a denominator to avoid a bias of sudden jump of the reference value at certain temperatures

748   where the number of available data changes. As shown in the figure, data deviation (i.e.,

749   scatter from the Avg. $\log(n_{s,\text{ind.}})/\log(n_{s,\text{fit}}) = 1$ line) can be seen in both suspension

750   measurements and dry aerosol measurements. This deviation is observed with all the $n_{s,\text{fit}}$

751   cases [All (log), Sus (log) and Dry (log)]. Additionally, the scatter of individual non-T-binned

752   data and the validity of interpolations are presented in Figs. S5-S8. In specific, these four

753   figures (Figs. S5-S8) complement panels a.ii and a.iii, panels b.ii and b.iii, panels a.iv and a.v

754   and panels b.iv and b.v. from Fig. S4, respectively, in greater detail.
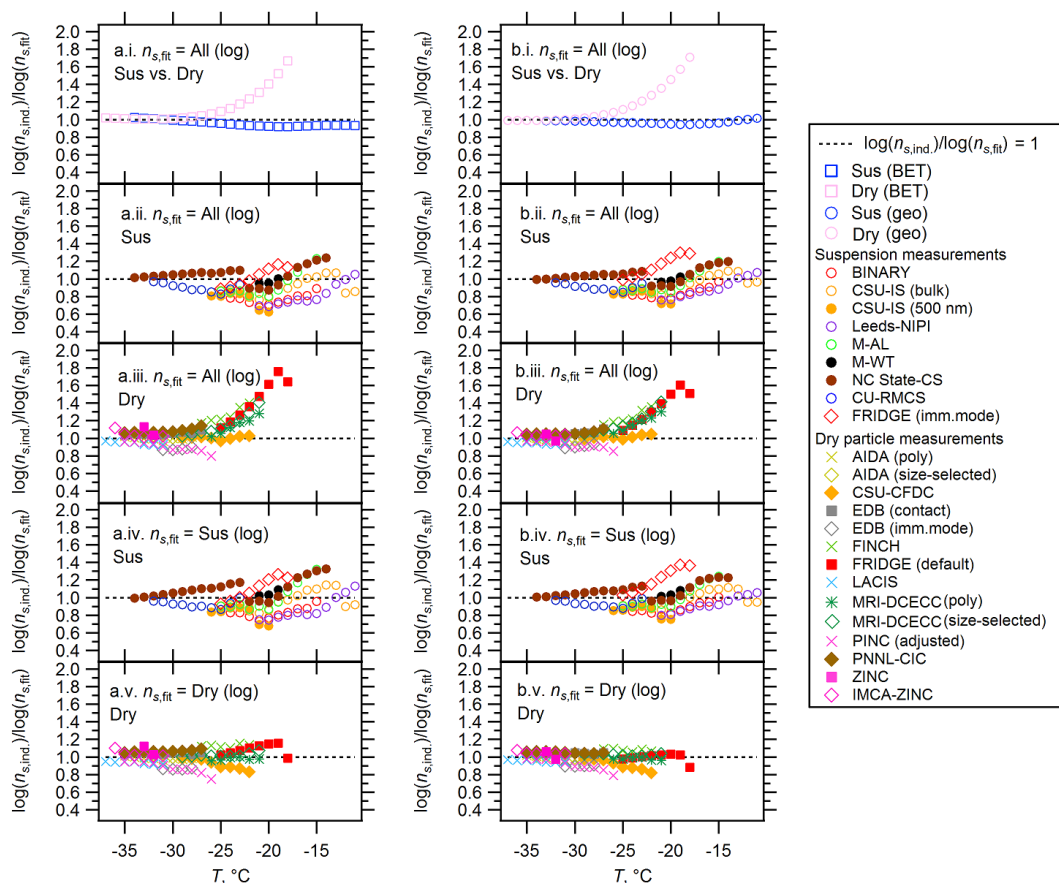
755
756   Figure S4. T-binned ratios of the interpolated individual measurements to the fit of the data, $\log(n_{s,\text{ind.}})/\log(n_{s,\text{fit}})$,
757   based on the BET (a) and geometric (b) surface area, across the temperature range covered for all the
758   measurement techniques used in the present study (i.e., 1 °C bins for -37 °C $< T <$ -11 °C). T-binned
759    $\log(n_{s,\text{ind.}})/\log(n_{s,\text{fit}})$ are presented for (i) ratios of the log fit to suspension measurements [Sus (log)] or dry-
760   dispersed particle measurements [Dry (log)] to the log fit to all the data [All (log)], (ii) ratios of the individual
761   suspension measurements to All (log), (iii) ratios of the individual dry-dispersed particle measurements to All
762   (log), (iv) ratios of the individual suspension measurements to Sus (log) and (v) ratios of the individual dry-
763   dispersed particle measurements to Dry (log). The black dotted line represents $\log(n_{s,\text{ind.}})/\log(n_{s,\text{fit}}) = 1$.
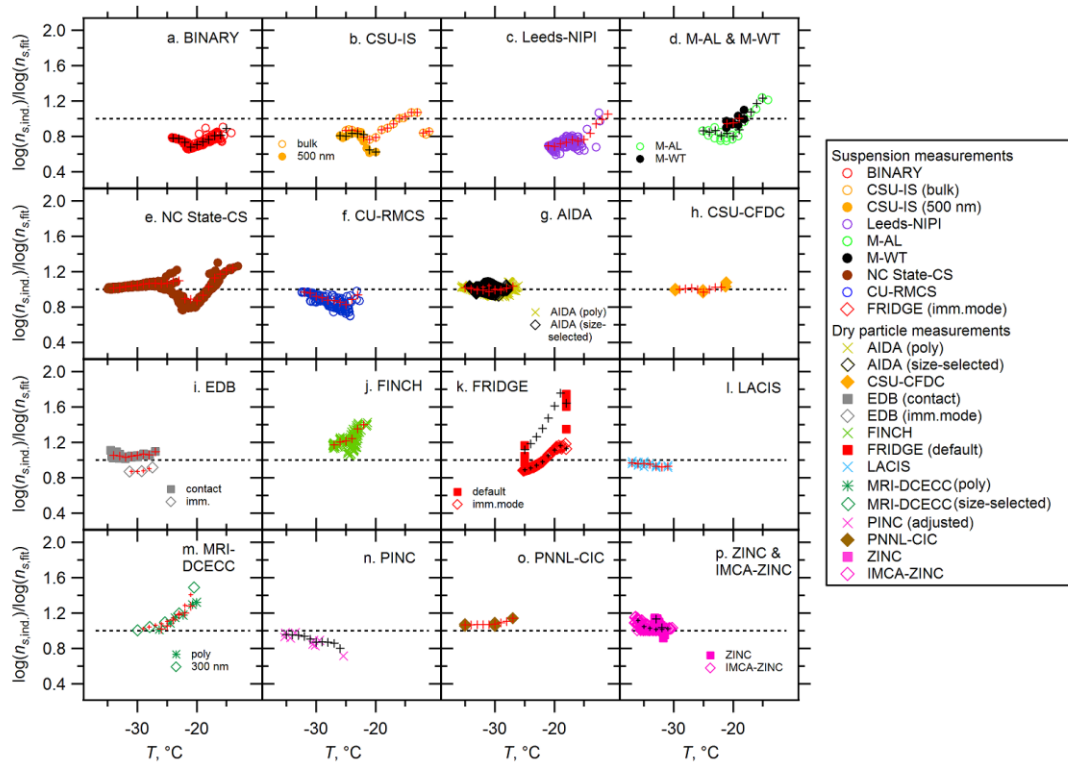
764
765 Figure S5. Ratios of the individual measurements to the log fit to all the data [All (log)], $\log(n_{s,\text{ind.}})/\log(n_{s,\text{fit}})$,
766 based on the BET surface area ($n_{s,\text{ind.}} = n_{s,\text{BET}}$). Black or red cross markers represent T-binned ratios of the
767 interpolated individual measurements to All (log) in comparison to the non-T-binned ratios. The black dotted line
768 represents $\log(n_{s,\text{ind.}})/\log(n_{s,\text{fit}}) = 1$.
769
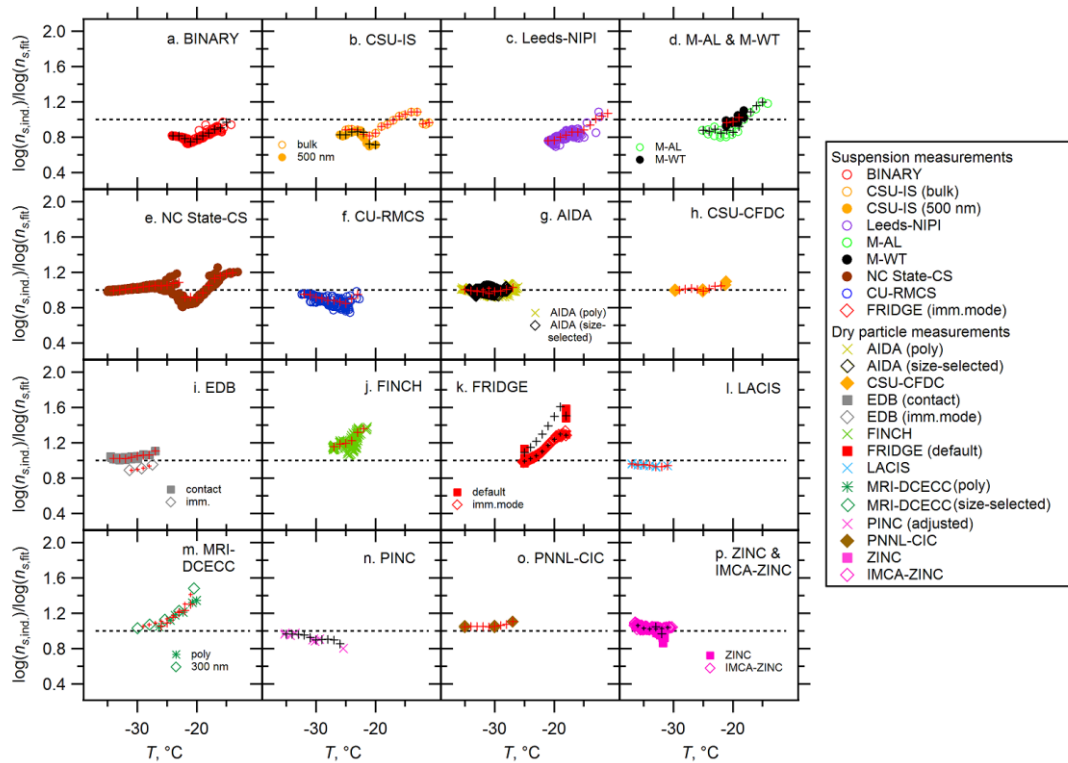
770
771 Figure S6. Ratios of the individual measurements to the log fit to all the data [All (log)], $\log(n_{s,\text{ind.}})/\log(n_{s,\text{fit}})$,
772 based on the geometric surface area ($n_{s,\text{ind.}} = n_{s,\text{geo}}$). Black or red cross markers represent T-binned ratios of the
773 interpolated individual measurements to All (log) in comparison to the non-T-binned ratios. The black dotted line
774 represents $\log(n_{s,\text{ind.}})/\log(n_{s,\text{fit}}) = 1$.
775
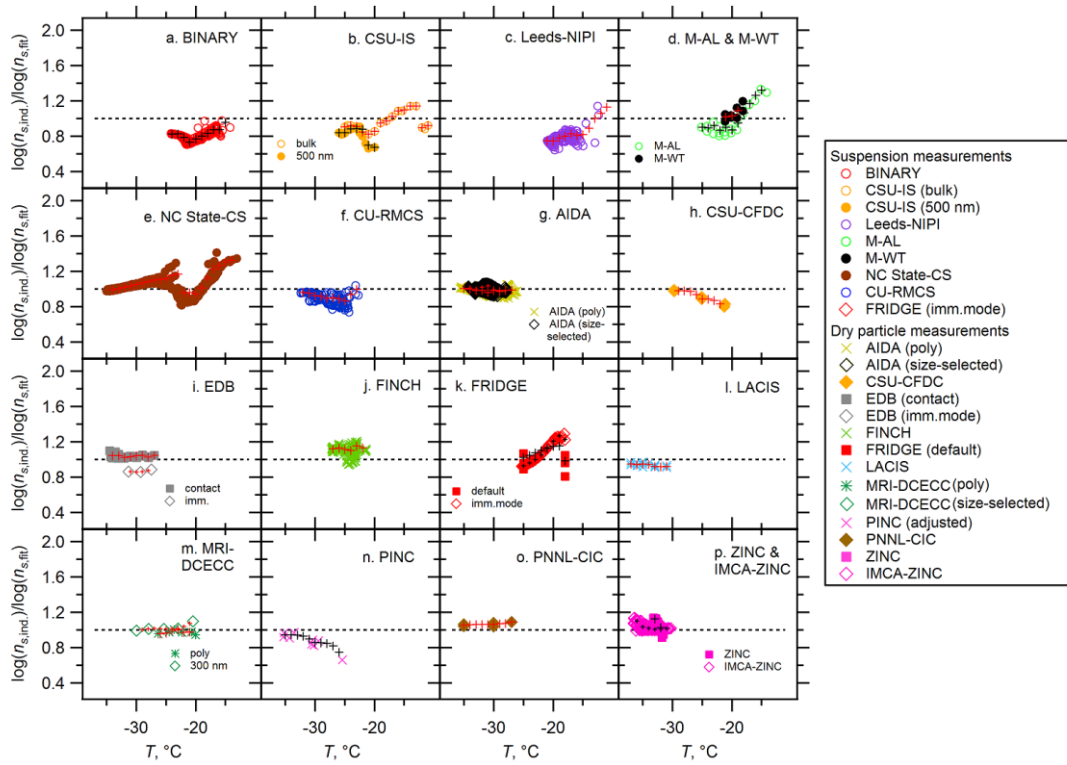
776
777 Figure S7. Ratios of the individual measurements to the log fit to suspension measurements [Sus (log)] or dry-
778 dispersed particle measurements [Dry (log)], $\log(n_{s,\text{ind.}})/\log(n_{s,\text{fit}})$, based on the BET surface area ($n_{s,\text{ind.}} = n_{s,\text{BET}}$).
779 Black or red cross markers represent T-binned ratios of the interpolated individual measurements to Sus (log) or
780 Dry (log) in comparison to the non-T-binned ratios. The black dotted line represents $\log(n_{s,\text{ind.}})/\log(n_{s,\text{fit}}) = 1$.
781
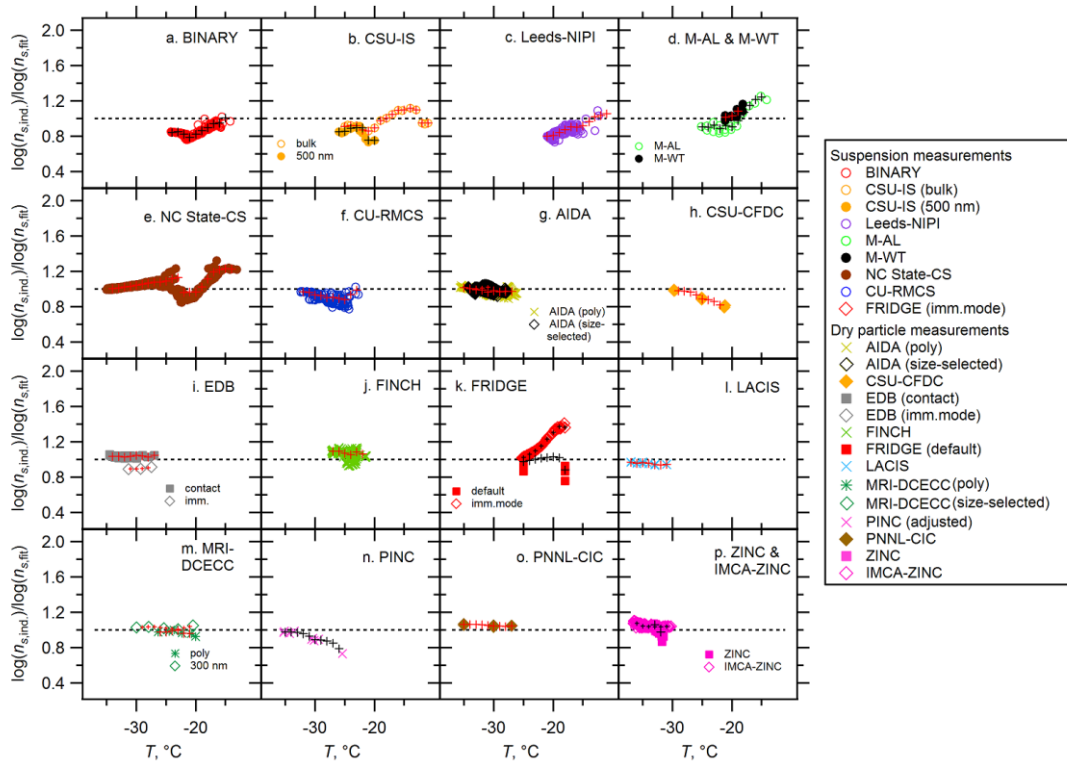
782
783 Figure S8. Ratios of the individual measurements to the log fit to suspension measurements [Sus (log)] or dry-
784 dispersed particle measurements [Dry (log)], $\log(n_{s,\text{ind.}})/\log(n_{s,\text{fit}})$, based on the geometric surface area ($n_{s,\text{ind.}} =$
785 $n_{s,\text{geo}}$). Black or red cross markers represent T-binned ratios of the interpolated individual measurements to Sus
786 (log) or Dry (log) in comparison to the non-T-binned ratios. The black dotted line represents $\log(n_{s,\text{ind.}})/\log(n_{s,\text{fit}})$
787 = 1.

29

S3.   Supplementary Table

789

790   A combination of four different methods for particle dispersion (rotating brush, flask

791   dispersion, fluidized bed, or disc-dispersion method) and four types of DMA [commercially

792   available one from TSI (Model 3081), Type Vienna Hauke medium (*Knutson and Whitby*,

793   1975) or custom built Maxi-DMA from TROPOS (*Raddatz et al*., 2013)] was employed for

794   particle generation of illite NX samples. Further, most of the dry dispersion techniques used

795   upstream impactors to filter out large agglomerated particles and safeguard against counting

796   these large particles as INPs. The different types of dispersion methods, impactors and size

797   segregating instruments used in the present work are listed below.

798

799   Table S1. Summary of methods used for dry particle generation.

Instrument	Dispersion method	Size selecting instrument	Impactor type
AIDA[*]	Rotating brush	TSI DMA 3081	Cyclone impactors (D_{50} 1 μm and 5 μm)
CSU-CFDC	Flask dispersion	TSI DMA 3081	Dual single-jet impactors (cutpoint of 1.5 and 2.4 μm)
EDB[*]	Fluidized bed	TSI DMA 3081	Multistage impactor (cutpoint of 2 μm)
FINCH[*]	Fluidized bed	DMA, type Vienna Hauke medium	MOUDI and cyclone impactors
FRIDGE (default)[*]	Rotating brush	TSI DMA 3081	Cyclone impactors (D_{50} 1 μm and 5 μm)
LACIS[*]	Fluidized bed	DMA, type Vienna Hauke medium	MOUDI and cyclone impactors
MRI-DCECC	Rotating brush	TSI DMA 3081	Cyclone impactors (D_{50} of 2.5 μm and 1.0 μm)
PINC	Rotating brush	TROPOS Maxi-DMA	Impactor (D_{50} at 0.91 μm)
PNNL-CIC	Rotating disc dispersion	TSI DMA 3081	Cyclone impactor (D_{50} ~1 μm)
IMCA-ZINC	Fluidized bed	TSI DMA 3081	Cyclone impactors (D_{50} 3 μm and 1 μm)

800   [*]Instruments of INUIT project partners.

S4.   **List of Abbreviations, Acronyms and Symbols (Alphabetical Order)**

802

803	AIDA:	Aerosol Interaction and Dynamics in the Atmosphere
804	All (lin):	multiple exponential fit to T-binned ensemble n_s dataset fitted in the linear
805		space
806	All (log):	multiple exponential fit to T-binned ensemble n_s dataset fitted in the log space
807	All$_{max}$:	multiple exponential fit to T-binned ensemble maximum n_s values
808	All$_{min}$:	multiple exponential fit to T-binned ensemble minimum n_s values
809	APS:	aerodynamic particle sizer
810	ATD:	Arizona Test Dust
811	A13:	Atkinson's parameterization
812	BET:	Brunauer, Emmett, and Teller
813	BINARY:	Bielefeld Ice Nucleation ARraY
814	B12:	Broadley's parameterization
815	CEC:	Cation Exchange Capacity
816	CECC:	controlled expansion cloud-simulation chamber
817	CFDC:	continuous flow diffusion chamber
818	$c_{impurities}(T)$:	concentration of impurities per unit volume water at temperature T
819	$c_{IN}(T)$:	concentration of INP per unit volume water at temperature T
820	CNT:	classical nucleation theory
821	CPC:	condensation particle counter
822	CSU-IS:	Colorado State University Ice Spectrometer
823	CSU-CFDC:	Colorado State University Continuous Flow Diffusion Chamber
824	CU-RMCS:	University of Colorado Raman microscope cold stage
825	DCECC:	Dynamic Controlled Expansion Cloud-simulation Chamber
826	DFG:	Deutsche Forschungsgemeinschaft (German Research Society)
827	$\Delta\log(n_s)/\Delta T$:	slope of $n_s(T)$ spectrum
828	DLS:	dynamic light scattering
829	DMA:	differential mobility analyzer
830	DSF:	dynamic shape factor
831	D:	average median diameter
832	Dry (lin):	multiple exponential fit to T-binned dry-dispersed particle n_s subset fitted in the
833		linear space
834	Dry (log):	multiple exponential fit to T-binned dry-dispersed particle n_s subset fitted in the
835		log space
836	D_{thresh}:	droplet-ice threshold diameter
837	D_{ve}:	volume equivalent midpoint diameter of individual particle
838	D_{50}:	cut size with a 50% mass of particles
839	D_{95}:	cut size with a 95% mass of particles
840	e_c:	probability of freezing on a single contact
841	EDB:	ElectroDynamic Balance
842	EDX:	energy dispersive X-ray
843	FINCH:	Fast Ice Nucleus CHamber
844	FRIDGE:	FRankfurt Ice Deposition freezinG Experiment
845	f:	proportion of droplets not frozen
846	f_{ice}:	frozen fraction after time t
847	f_{ice}^*:	fraction of droplets frozen
848	$f_{unfrozen}$:	fraction of unfrozen drops at each particular temperature

849	Hor$_{Max-Min}$:	horizontal T deviation between maxima and minima in $n_s(T)$ spectrum
850	IC:	ion chromatography
851	ICIS-2007:	international ice nucleation workshop in 2007
852	illite NX:	commercially available NX Nanopowder illite-rich dust from Arginotec
853	IMCA-ZINC:	Zurich Ice Nucleation Chamber with Immersion Mode Cooling-chAmber
854	IN	ice nucleation
855	INP:	ice-nucleating particle
856	INUIT:	Ice Nuclei research UnIT
857	IODE:	Ice Optical DEpolarization detector
858	K-feldspar:	potassium-rich feldspar
859	$K'(T)$:	cumulative INP concentration at a temperature T
860	LACIS:	Leipzig Aerosol Cloud Interaction Simulator
861	Leeds-NIPI:	Leeds Nucleation by Immersed Particles Instrument
862	$\log(n_{s,ind.})/\log(n_{s,fit})$:	
863		ratios of the individual measurements to the fit of the data
864	M-AL:	Mainz Acoustic Levitator
865	M-WT:	Mainz vertical Wind Tunnel
866	min:	minute
867	MRI-DCECC:	Meteorological Research Institute DCECC
868	M_{total}:	total mass concentration of particles
869	M_{ve}:	volume equivalent mass of individual particle
870	n_c:	collision rate
871	NC State-CS:	North Carolina State cold stage
872	N_{ae}:	number concentration of aerosols
873	$N_{droplet}$:	number concentration of droplets
874	N_{ice}:	number concentration of ice crystals
875	$n_{m,geo}$:	geometric mass-based ice-nucleating mass
876	$n_{m,sus}$:	ice-nucleating mass derived from suspension measurements
877	n_s:	IN active surface-site density
878	$n_{s,average}$:	average n_s
879	$n_{s,BET}$:	BET surface-inferred n_s
880	$n_{s,ind.}$:	individual n_s measurements
881	$n_{s,fit}$:	fit of all the $n_{s,ind.}$ data across the measured temperature range
882	$n_{s,geo}$:	geometric size based n_s
883	$n_{s,max}$:	maximum n_s
884	$n_{s,min}$:	minimum n_s
885	$N(T)$:	number of frozen droplets at temperature T
886	N_{total}:	total number concentration of particles
887	N_0:	total number of droplets
888	N12:	Niemand's parameterization
889	OPC:	optical particle counter
890	OPS:	optical particle sizer
891	PCR:	polymerase chain reaction
892	PDF:	probability density function
893	PDMS:	polydimethylsiloxane
894	PINC:	Portable Ice Nucleation Chamber
895	PNNL-CIC:	Pacific Northwest National Laboratory Compact Ice Chamber
896	r:	correlation coefficient
897	RH$_{ice}$:	relative humidity with respect to ice
898	RH$_w$:	relative humidity with respect to water
899	RH$_{w,ds}$:	RH$_w$ at which droplets survive past the evaporation section

900	s:	second
901	SBM:	soccer ball model
902	SIMONE:	German acronym of *Streulicht-intensitätsmessungen zum optischen Nachweis*
903		*von Eispartikeln*, which translates to the scattering intensity measurement for
904		the optical detection of ice
905	S_{IN}:	surface area of a single ice-nucleating particle
906	SMPS:	scanning mobility particle sizer
907	SSA:	specific surface area
908	SSPD:	small-scale powder disc-disperser
909	S_{total}:	total surface area concentration of particles
910	Sus (lin):	multiple exponential fit to T-binned suspension n_s subset fitted in the linear
911		space
912	Sus (log):	multiple exponential fit to T-binned suspension n_s subset fitted in the log space
913	S_{ve}:	volume equivalent surface area of individual particle
914	t:	time
915	T:	temperature
916	T-binned Lin. Avg.:	
917		multiple exponential distribution fit to the T-binned average data in the linear
918		space
919	T-binned Log. Avg:	
920		multiple exponential distribution fit to the T-binned average data in the log
921		space
922	T-binned Max.: fit to the T-binned maxima in the linear space	
923	T-binned Min.: fit to the T-binned minima in the linear space	
924	TDL:	tunable diode laser
925	$T_{drop}(t)$:	drop surface temperature
926	$T_{droplet,onset}$:	droplet onset temperature
927	TROPOS:	Leibniz Institute for Tropospheric Research
928	UHSAS:	Ultra-High Sensitivity Aerosol Spectrometer
929	V:	droplet volume
930	V_{drop}:	median drop volume of the population
931	$Ver_{Max-Min}$:	vertical n_s deviation between maxima and minima in $n_s(T)$ spectrum
932	w:	mass ratio of dust and water (g dust/g water)
933	wt%:	weight percent
934	x:	volume of water used to wash the particles from the filter
935	XRD:	X-ray diffraction
936	y:	volume of air sampled through the filter
937	α:	ice activated fraction (= N_{ice}/N_{total})
938	θ:	specific surface area measured by BET technique
939	θ_{N2}:	specific surface area measured by BET technique with nitrogen gas
940	θ_{H2O}:	specific surface area measured by BET technique with water vapor
941	ρ:	particle density of illite NX
942	ρ_w:	density of water (0.9971 g H_2O/m^3 H_2O)
943	χ:	dynamic shape factor

References

Agresti, A. and Coull, B. A.: Approximate is better than "exact" for interval estimation of binomial proportions. Am. Stat., 52, 119–126, doi:10.2307/2685469, 1998.

Ardon-Dryer, K. and Levin, Z.: Ground-based measurements of immersion freezing in the eastern Mediterranean, Atmos. Chem. Phys., 14, 5217–5231, doi:10.5194/acp-14-5217-2014, 2014.

Atkinson, J. D., Murray, B. J., Woodhouse, M. T., Carslaw, K., Whale, T. F., Baustian, K., Dobbie, S., O'Sullivan, D., and Malkin, T. L.: Nature, 498, 355–358, doi:10.1038/nature12278, 2013.

Baustian, K. J., Wise, M. E., and Tolbert, M. A.: Depositional ice nucleation on solid ammonium sulfate and glutaric acid particles, Atmos. Chem. Phys., 10, 2307–2317, doi:10.5194/acp-10-2307-2010, 2010.

Benz, S., Megahed, K., Möhler, O., Saathoff, H., Wagner, R., and Schurath, U.: T-dependent rate measurements of homogeneous ice nucleation in cloud droplets using a large atmospheric simulation chamber, J. Photoch. Photobio. A, 176, 208–217, doi:10.1016/j.jphotochem.2005.08.026, 2005.

Broadley, S. L., Murray, B. J., Herbert, R. J., Atkinson, J. D., Dobbie, S., Malkin, T. L., Condliffe, E., and Neve, L.: Immersion mode heterogeneous ice nucleation by an illite rich powder representative of atmospheric mineral dust, Atmos. Chem. Phys., 12, 287–307, doi:10.5194/acp-12-287-2012, 2012.

Budke, C. and Koop, T.: BINARY: an optical freezing array for assessing temperature and time dependence of heterogeneous ice nucleation, Atmos. Meas. Tech. Discuss., 7, 9137–9172, doi:10.5194/amtd-7-9137-2014, 2014.

Bundke, U., Nillius, B., Jaenicke, R., Wetter, T., Klein, H., and Bingemer, H.: The fast ice nucleus chamber FINCH, Atmos. Res., 90, 180–186, doi:10.1016/j.atmosres.2008.02.008, 2008.

Bundke, U., Reimann, B., Nillius, B., Jaenicke, R., and Bingemer, H.: Development of a Bioaerosol single particle detector (BIO IN) for the Fast Ice Nucleus CHamber FINCH, Atmos. Meas. Tech., 3, 263–271, doi:10.5194/amt-3-263-2010, 2010.

Chou, C., Stetzer, O., Weingartner, E., Jurányi, Z., Kanji, Z. A., and Lohmann, U.: Ice nuclei properties within a Saharan dust event at the Jungfraujoch in the Swiss Alps, Atmos. Chem. Phys., 11, 4725–4738, doi:10.5194/acp-11-4725-2011, 2011.

Clauss, T., Kiselev, A., Hartmann, S., Augustin, S., Pfeifer, S., Niedermeier, D., Wex, H., and Stratmann, F.: Application of linear polarized light for the discrimination of frozen and liquid droplets in ice nucleation experiments, Atmos. Meas. Tech., 6, 1041–1052, doi:10.5194/amt-6-1041-2013, 2013.

998   DeMott, P. J. and Coauthors: Resurgence in ice nuclei measurement research, B. Am.
999   Meteorol. Soc., 92, 1623–1635, doi:http://dx.doi.org/10.1175/2011BAMS3119.1, 2011.
1000

1001   DeMott, P. J., Prenni, A. J., McMeeking, G. R., Sullivan, R. C., Petters, M. D., Tobo, Y.,
1002   Niemand, M., Möhler, O., Snider, J. R., Wang, Z., and Kreidenweis, S. M.: Integrating
1003   laboratory and field data to quantify the immersion freezing ice nucleation activity of mineral
1004   dust particles, Atmos. Chem. Phys. Discuss., 14, 17359–17400, doi:10.5194/acpd-14-17359-
1005   2014, 2014.
1006

1007   Diehl, K., Mitra, S. K., Szakáll, M., Blohn, N. v., Borrmann, S., and Pruppacher, H.R.:
1008   Chapter 2. Wind Tunnels: Aerodynamics, Models, and Experiments. In: The Mainz Vertical
1009   Wind Tunnel Facility: A Review of 25 Years of Laboratory Experiments on Cloud Physics
1010   and Chemistry [Pereira, J. D. (eds.)], Nova Science Publishers, Inc., Hauppauge, NY, USA,
1011   2011.
1012

1013   Diehl, K., Debertshäuser, M., Eppers, O., Schmithüsen, H., Mitra, S.K., and Borrmann, S.:
1014   Particle-area dependence of mineral dust in the immersion mode: investigations with freely
1015   suspended drops in an acoustic levitator. Atmos. Chem. Phys., 14, 12343–12355,
1016   doi:10.5194/acp-14-12343-2014, 2014.
1017

1018   Eidhammer, T., DeMott, P. J., Prenni, A. J., Petters, M. D., Twohy, C. H., Rogers, D. C.,
1019   Stith, J., Heymsfield, A., Wang, Z., Haimov, S., French, J., Pratt, K., Prather, K., Murphy, S.,
1020   Seinfeld, J., Subramanian, R., and Kreidenweis, S. M.: Ice initiation by aerosol particles:
1021   Measured and predicted ice nuclei concentrations versus measured ice crystal concentrations
1022   in an orographic wave cloud. J. Atmos. Sci., 67, 2417–2436. doi: 10.1175/2010JAS3266.1,
1023   2010.
1024

1025   Fahey, D. W., Gao, R.-S., Möhler, O., Saathoff, H., Schiller, C., Ebert, V., Krämer, M., Peter,
1026   T., Amarouche, N., Avallone, L. M., Bauer, R., Bozóki, Z., Christensen, L. E., Davis, S. M.,
1027   Durry, G., Dyroff, C., Herman, R. L., Hunsmann, S., Khaykin, S. M., Mackrodt, P., Meyer, J.,
1028   Smith, J. B., Spelten, N., Troy, R. F., Vömel, H., Wagner, S., and Wienhold, F. G.: The
1029   AquaVIT-1 intercomparison of atmospheric water vapor measurement techniques, Atmos.
1030   Meas. Tech. Discuss., 7, 3159–3251, doi:10.5194/amtd-7-3159-2014, 2014.
1031

1032   Friedman, B., Kulkarni, G., Beránek, J., Zelenyuk, A., Thornton, J. A., and Cziczo, D. J.: Ice
1033   nucleation and droplet formation by bare and coated soot particles, J. Geophys. Res., 116,
1034   D17203, doi:10.1029/2011JD015999, 2011.
1035

1036   Hader, J. D., Wright, T. P., and Petters, M. D.: Contribution of pollen to atmospheric ice
1037   nuclei concentrations, Atmos. Chem. Phys., 14, 5433–5449, doi:10.5194/acp-14-5433-2014,
1038   2014.
1039

1040   Hartmann, S., Niedermeier, D., Voigtländer, J., Clauss, T., Shaw, R. A., Wex, H., Kiselev, A.,
1041   and Stratmann, F.: Homogeneous and heterogeneous ice nucleation at LACIS: operating
1042   principle and theoretical studies, Atmos. Chem. Phys., 11, 1753–1767, doi:10.5194/acp-11-
1043   1753-2011, 2011.
1044

1045   Herbert, R. J., Murray, B. J., Whale, T. F., Dobbie, S. J., and Atkinson, J. D.: Representing
1046   time-dependent freezing behaviour in immersion mode ice nucleation, Atmos. Chem. Phys.,
1047   14, 8501–8520, doi:10.5194/acp-14-8501-2014, 2014.
1048

1049   Hiranuma, N., Paukert, M., Steinke, I., Zhang, K., Kulkarni, G., Hoose, C., Schnaiter, M.,
1050   Saathoff, H., and Möhler, O.: A comprehensive parameterization of heterogeneous ice
1051   nucleation of dust surrogate: laboratory study with hematite particles and its application to
1052   atmospheric models, Atmos. Chem. Phys., 14, 13145–13158, doi:10.5194/acp-14-13145-
1053   2014, 2014a.
1054
1055   Hiranuma, N., Hoffmann, N., Kiselev, A., Dreyer, A., Zhang, K., Kulkarni, G., Koop, T., and
1056   Möhler, O.: Influence of surface morphology on the immersion mode ice nucleation
1057   efficiency of hematite particles, Atmos. Chem. Phys., 14, 2315–2324, doi:10.5194/acp-14-
1058   2315-2014, 2014b.
1059
1060   Hoffmann, N., Duft, D., Kiselev, A., and Leisner, T.: Contact freezing efficiency of mineral
1061   dust aerosols studied in an electrodynamic balance: quantitative size and temperature
1062   dependence for illite particles, Faraday Discuss., 165, 383–390, doi:10.1039/C3FD00033H,
1063   2013a.
1064
1065   Hoffmann, N., Kiselev, A., Rzesanke, D., Duft, D., and Leisner, T.: Experimental
1066   quantification of contact freezing in an electrodynamic balance, Atmos. Meas. Tech., 6, 2373–
1067   2382, doi:10.5194/amt-6-2373-2013, 2013b.
1068
1069   Hu, Y.-X., Yang, P., Lin, B., Gibson, G., Hostetler, C.: Discriminating between spherical and
1070   non-spherical scatterers with lidar using circular polarization: a theoretical study. J. Quant.
1071   Spectrosc. Radiat. Transfer, 79–80, 757–764, doi:10.1016/S0022-4073(02)00320-5, 2003.
1072
1073   Kanji, Z. A., Welti, A., Chou, C., Stetzer, O., and Lohmann, U.: Laboratory studies of
1074   immersion and deposition mode ice nucleation of ozone aged mineral dust particles, Atmos.
1075   Chem. Phys., 13, 9097–9118, doi:10.5194/acp-13-9097-2013, 2013.
1076
1077   Klein, H., Haunold, W., Bundke, U., Nillius, B., Wetter, T., Schallenberg, S., and Bingemer,
1078   H.: A new method for sampling of atmospheric ice nuclei with subsequent analysis in a static
1079   diffusion chamber, Atmos. Res., 96, 218–224, doi:10.1016/j.atmosres.2009.08.002, 2010.
1080
1081   Knutson, E. O., and Whitby, K. T.: Aerosol classification by electric mobility: apparatus,
1082   theory, and applications. Aerosol Sci., 6, 6, 443–451, doi:10.1016/0021-8502(75)90060-9,
1083   1975.
1084
1085   Kulkarni, G., Fan, J., Comstock, J. M., Liu, X., and Ovchinnikov, M.: Laboratory
1086   measurements and model sensitivity studies of dust deposition ice nucleation, Atmos. Chem.
1087   Phys., 12, 7295–7308, doi:10.5194/acp-12-7295-2012, 2012.
1088
1089   Langham, E. J. and Mason, B. J.: The heterogeneous and homogeneous nucleation of
1090   supercooled water. Proceedings of the Royal Society A: Mathematical, Physical and
1091   Engineering Sciences, 247, 1251, 493–504. doi:10.1098/rspa.1958.0207, 1958.
1092
1093   Lüönd, F., Stetzer, O., Welti, A., and Lohmann, U.: Experimental study on the ice nucleation
1094   ability of size-selected kaolinite particles in the immersion mode, J. Geophys. Res., 115,
1095   D14201, doi:10.1029/2009JD012959, 2010.
1096
1097   Möhler, O., Stetzer, O., Schaefers, S., Linke, C., Schnaiter, M., Tiede, R., Saathoff, H.,
1098   Krämer, M., Mangold, A., Budz, P., Zink, P., Schreiner, J., Mauersberger, K., Haag, W.,
1099   Kärcher, B., and Schurath, U.: Experimental investigation of homogeneous freezing of

1100 sulphuric acid particles in the aerosol chamber AIDA, Atmos. Chem. Phys., 3, 211–223,
1101 doi:10.5194/acp-3-211-2003, 2003.
1102
1103 Möhler, O., Field, P. R., Connolly, P., Benz, S., Saathoff, H., Schnaiter, M., Wagner, R.,
1104 Cotton, R., Krämer, M., Mangold, A., and Heymsfield, A. J.: Efficiency of the deposition
1105 mode ice nucleation on mineral dust particles, Atmos. Chem. Phys., 6, 3007–3021,
1106 doi:10.5194/acp-6-3007-2006, 2006.
1107
1108 Murphy, D. M., and Koop, T.: Review of the vapour pressures of ice and supercooled water
1109 for atmospheric applications, Q. J. R. Meteorol. Soc., 131, 1539–1565, doi:10.1256/qj.04.94,
1110 2005.
1111
1112 Murray, B. J., Broadley, S. L., Wilson, T. W., Atkinson, J. D., and Wills, R. H.:
1113 Heterogeneous freezing of water droplets containing kaolinite particles, Atmos. Chem. Phys.,
1114 11, 4191–4207, doi:10.5194/acp-11-4191-2011, 2011.
1115
1116 Murray, B. J., O'Sullivan, D., Atkinson, J. D., and Webb, M. E.: Ice nucleation by particles
1117 immersed in supercooled cloud droplets, Chem. Soc. Rev., 41, 6519–6554,
1118 doi:10.1039/c2cs35200a, 2012.
1119
1120 Nicolet, M., Stetzer, O., Lüönd, F., Möhler, O., and Lohmann, U.: Single ice crystal
1121 measurements during nucleation experiments with the depolarization detector IODE, Atmos.
1122 Chem. Phys., 10, 313–325, doi:10.5194/acp-10-313-2010, 2010.
1123
1124 O'Sullivan, D., Murray, B. J., Malkin, T. L., Whale, T. F., Umo, N. S., Atkinson, J. D., Price,
1125 H. C., Baustian, K. J., Browse, J., and Webb, M. E.: Ice nucleation by fertile soil dusts:
1126 relative importance of mineral and biogenic components, Atmos. Chem. Phys., 14, 1853–
1127 1867, doi:10.5194/acp-14-1853-2014, 2014.
1128
1129 Petters, M. D., Parsons, M. T., Prenni, A. J., DeMott, P. J., Kreidenweis, S. M., Carrico, C.
1130 M., Sullivan, A. P., McMeeking, G. R., Levin, E., Wold, C. E., Collett, J. L. Jr., and
1131 Moosmüller, H.: Ice nuclei emissions from biomass burning, J. Geophys. Res., 114, D07209,
1132 doi:10.1029/2008JD011532, 2009.
1133
1134 Prenni, A. J., DeMott, P. J., Rogers, D. C., Kreidenweis, S. M., McFarquhar, G. M., Zhang,
1135 G., and Poellot, M. R.: Ice nuclei characteristics from M-PACE and their relation to ice
1136 formation in clouds, Tellus, 61B, 436–448, doi:10.1111/j.1600-0889.2009.00415.x, 2009.
1137
1138 Raddatz, M., Wiedensohler, A., Wex, H., and Stratmann, F.: Size selection of sub- and super-
1139 micron clay mineral kaolinite particles using a custom-built Maxi-DMA, AIP Conference
1140 Proceedings, 1527, 457–460, 2013.
1141
1142 Richardson, M.: Making real time measurements of ice nuclei concentrations at upper
1143 tropospheric temperatures: Extending the capabilities of the continuous flow diffusion
1144 chamber, DISSERTATION thesis, Colorado State Univ., Fort Collins, CO, USA, 268 pp,
1145 2009.
1146
1147 Rzesanke, D., Nadolny, J., Duft, D., Muller, R., Kiselev, A., and Leisner, T.: On the role of
1148 surface charges for homogeneous freezing of supercooled water microdroplets, Phys. Chem.
1149 Chem. Phys., 14, 9359–9363, doi:10.1039/c2cp23653b, 2012.
1150

1151 Rogers, D. C.: Development of a continuous flow thermal gradient diffusion chamber for ice
1152 nucleation studies, Atmos. Res., 22, 149–181, doi:10.1016/0169-8095(88)90005-1, 1988.
1153

1154 Rogers, D. C., DeMott, P. J., Kreidenweis, S. M., and Chen, Y.: A continuous-flow diffusion
1155 chamber for airborne measurements of ice nuclei, J. Atmos. Oceanic Technol., 18, 725–741,
1156 doi:http://dx.doi.org/10.1175/1520-0426(2001)018<0725:ACFDCF>2.0.CO;2, 2001.
1157

1158 Schill, G. P. and Tolbert, M. A.: Heterogeneous ice nucleation on phase-separated organic-
1159 sulfate particles: effect of liquid vs. glassy coatings, Atmos. Chem. Phys., 13, 4681–4695,
1160 doi:10.5194/acp-13-4681-2013, 2013.
1161

1162 Schnaiter, M., Büttner, S., Möhler, O., Skrotzki, J., Vragel, M., and Wagner, R.: Influence of
1163 particle size and shape on the backscattering linear depolarisation ratio of small ice crystals –
1164 cloud chamber measurements in the context of contrail and cirrus microphysics, Atmos.
1165 Chem. Phys., 12, 10465–10484, doi:10.5194/acp-12-10465-2012, 2012.
1166

1167 Steinke, I., Möhler, O., Kiselev, A., Niemand, M., Saathoff, H., Schnaiter, M., Skrotzki, J.,
1168 Hoose, C., and Leisner, T.: Ice nucleation properties of fine ash particles from the
1169 Eyjafjallajökull eruption in April 2010, Atmos. Chem. Phys., 11, 12945–12958,
1170 doi:10.5194/acp-11-12945-2011, 2011.
1171

1172 Stetzer, O., Baschek, B., Luond, F., and Lohmann, U.: The Zurich Ice Nucleation Chamber
1173 (ZINC) – A new instrument to investigate atmospheric ice formation, Aerosol Sci. Technol.,
1174 42, 64–74, doi:10.1080/02786820701787944, 2008.
1175

1176 Sullivan, R. C., Petters, M. D., DeMott, P. J., Kreidenweis, S. M., Wex, H., Niedermeier, D.,
1177 Hartmann, S., Clauss, T., Stratmann, F., Reitz, P., Schneider, J., and Sierau, B.: Irreversible
1178 loss of ice nucleation active sites in mineral dust particles caused by sulphuric acid
1179 condensation, Atmos. Chem. Phys., 10, 11471–11487, doi:10.5194/acp-10-11471-2010,
1180 2010a.
1181

1182 Sullivan, R. C., Miñambres, L., DeMott, P. J., Prenni, A. J., Carrico, C. M., Levin, E. J. T.,
1183 and Kreidenweis, S. M.: Chemical processing does not always impair heterogeneous ice
1184 nucleation of mineral dust particles, Geophys. Res. Lett., 37, L24805,
1185 doi:10.1029/2010GL045540, 2010b.
1186

1187 Szakáll, M., Diehl, K., Mitra, S. K., and Borrmann, S.: A wind tunnel study on the shape,
1188 oscillation, and internal circulation of large raindrops with sizes between 2.5 and 7.5 mm, J.
1189 Atmos. Sci., 66, 755–765, doi:http://dx.doi.org/10.1175/2008JAS2777.1, 2009.
1190

1191 Tajiri, T., Yamashita, K., Murakami, M., Orikasa, N., Saito, A., Kusunoki, K., and Lilie, L.: A
1192 novel adiabatic-expansion-type cloud simulation chamber. J. Meteor. Soc. Japan, 91, 5, 687–
1193 704, doi:http://dx.doi.org/10.2151/jmsj.2013-509, 2013.
1194

1195 Tobo, Y., DeMott, P. J., Hill, T. C. J., Prenni, A. J., Swoboda-Colberg, N. G., Franc, G. D.,
1196 and Kreidenweis, S. M.: Organic matter matters for ice nuclei of agricultural soil origin,
1197 Atmos. Chem. Phys. Discuss., 14, 9705–9728, doi:10.5194/acpd-14-9705-2014, 2014.
1198

1199 Vali, G.: Quantitative evaluation of experimental results an the heterogeneous freezing
1200 nucleation of supercooled liquids. J. Atmos. Sci., 28, 402–409.
1201 doi:http://dx.doi.org/10.1175/1520-0469(1971)028<0402:QEOERA>2.0.CO;2, 1971.

1202

1203 Welti, A., Lüönd, F., Stetzer, O., and Lohmann, U.: Influence of particle size on the ice
1204 nucleating ability of mineral dusts, Atmos. Chem. Phys., 9, 6705–6715, doi:10.5194/acp-9-
1205 6705-2009, 2009.
1206

1207 Wex, H., DeMott, P. J., Tobo, Y., Hartmann, S., Rösch, M., Clauss, T., Tomsche, L.,
1208 Niedermeier, D., and Stratmann, F.: Kaolinite particles as ice nuclei: learning from the use of
1209 different kaolinite samples and different coatings, Atmos. Chem. Phys., 14, 5529–5546,
1210 doi:10.5194/acp-14-5529-2014, 2014.
1211

1212 Wright, T. P. and Petters, M. D.: The role of time in heterogeneous freezing nucleation, J.
1213 Geophys. Res. Atmos., 118, 3731–3743, doi:10.1002/jgrd.50365, 2013.